Evaluation of Morison approach with CFD modelling on a surface-piercing cylinder towards the investigation of FOWT Hydrodynamics

Constance Clément, Pauline Bozonnet, Guillaume Vinay, Philippe Pagnier, Adria Borras Nadal, Julien Reveillon

Evaluation of Morison approach with CFD modelling on a surface-piercing cylinder towards the investigation of FOWT Hydrodynamics

Constance Clément[a,c,*], Pauline Bozonnet[a], Guillaume Vinay[b], Philippe Pagnier[a], Adria Borras Nadal[b], Julien Réveillon[c]

Dedicated to the memory of Philippe Pagnier (1966-2021)

[a] *IFP Energies nouvelles, Solaize, France*
[b] *IFP Energies nouvelles, Rueil-Malmaison, France*
[c] *CORIA-UMR6614, Normandie Université, Université and INSA de Rouen, CNRS, Saint Etienne du Rouvray, France*

Abstract

To predict hydrodynamic forces on slender cylinders, Morison formula is commonly used. The expression is composed of two terms including an empirical drag and inertia coefficient. In the present study, a constrained cylinder subjected to regular waves is modelled using Computational Fluid Dynamics (CFD) and Morison coefficients are derived from the CFD loads.

A numerical wave tank, including a surface-piercing cylinder, is implemented to generate, propagate and absorb waves in a controlled way. The cylinder is discretised into slices for each of which the Morison formulation is fitted to the CFD loads to determine Morison coefficients.

Morison formulation is in very good agreement with the numerical load over the entire length of the cylinder, except for the slices near the free surface which are outside the applicability range of Morison formula. The loads near the free surface being negligible compared to the total load, the total theoretical load obtained reproduces well the experimental and the CFD loads.

The CFD simulations proved to be a powerful tool to predict the wave loads and calibrate Morison coefficients. On this basis, the methodology will be extended to floating offshore wind platforms, combining several cylinders with different inclinations, sizes and positions.

Keywords: Surface-piercing cylinder, Numerical Wave Tank, OpenFOAM, Computational Fluid Dynamics, Floating Offshore Wind Turbines, Morison empirical formula.

*Corresponding author, constanceclement120@hotmail.fr

1. Introduction

Offshore wind capacity has been steadily increasing over the last two decades, reaching a total installed capacity of 35.3 GW by the end of 2020 (see GWEC (2021)). Currently, the most common type of offshore wind turbine is the bottom-fixed wind turbine. However, Floating Offshore Wind Turbines (FOWT) are developing and several pre-commercial installations exist, such as Hywind Scotland (30 MW) which has been operating since 2017 or WindFloat Atlantic (30 MW) in Portugal which has been operating since July 2020. FOWTs have many advantages over their fixed counterpart, as pointed out by Sarmiento and Guanche (2018). First, they are less sensitive to water depth than bottom-mounted turbines, which are limited to shallow waters only (depths below 40 m). This increases the number of possible installation sites and extends the potential of offshore wind. Secondly, the wind is more stable and higher away from the coast and can be more easily predicted. This allows for better control of electricity production and facilitates grid management. The turbine can be assembled at dockside and then towed to the site with standard vessels, reducing installation time compared to bottom-mounted offshore turbines. To design FOWTs, aero-hydro-servo-elastic solvers are commonly used to simulate the behaviour of the complex floater/wind turbine system under wind and wave conditions. These innovative tools are able to model coupled interactions such as the aerodynamic impact on mooring line fatigue or, conversely, the impact of platform motion on aerodynamic loads.

Two theories are applied to model the hydrodynamic loads on FOWTs: the linear potential flow theory and the empirical Morison formula. Depending on the ratio between the diameter of the structure (D) and the wavelength (λ) of the wave considered, one of the two theories or a combination of both is applied. For large buoys ($D >> \lambda$), the linear potential flow theory is used assuming that the flow is irrotational, homogeneous and non-viscous (Massie and Journée (2001)). For small structures ($D << \lambda$) such as braces connecting larger buoys, the loads are predicted with the empirical formula of Morison et al. (1950). This theory takes into account the viscous effect and flow separation. More precisely, the formula is composed of two terms: one term including the drag coefficient (C_D) and another including the inertia coefficient (C_M). The Morison coefficients are derived from experimental databases, determined in the 1980s. The experiments could consist of a horizontal cylinder in a vertical U-tube in which the water oscillates, a constrained cylinder subjected to waves, or a cylinder subjected to forced oscillations in still water (Sarpkaya (1977) and Chakrabarti (1979)). The coefficients are given in empirical databases in terms of dimensionless numbers such as Keulegan-Carpenter (Keulegan et al. (1958)), Reynolds and the ratio of the two called β or frequency coefficient. These numbers relate the characteristics of the structure (diameter, frequency and amplitude of oscillating motion) to the characteristics of the flow (amplitude and period of the wave).

Originally used for offshore oil and gas systems, the extension of Morison's empirical formula to FOWT can lead to a non-optimised design. Certain assumptions are generally considered for simplicity and robustness, such as using a single set of coefficients regardless of sea state and for all braces. Morison's coefficients may depend on the dimensions of the FOWT braces and buoys (diameter and length) as well as the characteristics

of the flow (amplitude, period, water depth). It is questionable whether these empirical databases and their usual implementation are accurate enough in the context of FOWT design (higher economic constraints, lower safety constraints). In addition, specific aspects are neglected in Morison's coefficients such as the proximity of the considered part of the floater to the free surface, the interaction between the braces, the orientation of the braces and the motion of the floater.
Such limits inherent to the simplified methods implemented in design tools and practical constraints while running design loops may be investigated and evaluated using Computational Fluid Dynamics (CFD). Indeed, CFD simulations provide a high-fidelity analysis of the loads and access to local information that may not be reachable by experiments (pressure and velocity fields, load distributions on specific parts of the floater...). CFD offers the advantage of easily setting and varying simulation conditions (wave characteristics, floater geometry). With CFD, the behaviour of a FOWT in waves can be modelled to investigate hydrodynamic limitations/uncertainties such as Morison applicability for FOWT load prediction.

To design a FOWT system and evaluate the hydrodynamic response of the floater, a sequence of simplified tests is usually performed with design tools or during model test campaigns. These tests can also be performed with CFD: constrained floater subjected to waves (see Sarlak et al. (2018), Wang et al. (2020a) and Benitz et al. (2015)), forced oscillations in calm water (see Tao et al. (2004); Tao and Cai (2004); Tao et al. (2007), Zhang and Ishihara (2018) and Pan and Ishihara (2019)), decay tests (see Sarlak et al. (2018), Borràs Nadal and Bozonnet (2020), Bruinsma (2016) and Burmester et al. (2017)) and finally free motion in waves (see Rivera-Arreba et al. (2019), Wang et al. (2020b) and Tran and Kim (2015)). The tests on the constrained floater subjected to waves are performed to study the hydrodynamic loads and especially the applicability of Morison's formula.

To perform such tests in CFD, a specific CFD model is set up, called a Numerical Wave Tank (NWT). It is based on the resolution of the Navier-Stokes equations, combined with an accurate wave generator and absorber. In OpenFOAM (Greenshields (2020)), two different methods are available to generate and absorb waves: a passive method using relaxation zones (`waveFoam` by Jacobsen (2017)) and an active method without relaxation zones (`olaFlow` by Higuera et al. (2015)). Windt et al. (2019), comparing the two methods, demonstrate that in deep water, the passive method is more appropriate than the active method, originally developed for shallow water. However, the relaxation method has a higher computational cost due to the large passive areas.
Several papers focus on the implementation of a surface-piercing cylinder in a NWT. Miquel et al. (2018) propagate waves on a constrained cylinder whose diameter makes it a large object relative to the incident waves. A passive and an active absorption method are compared. They conclude that the reflection in the tank does not significantly impact the peak-to-peak forces on the cylinder. Nevertheless, the wave force peaks reached with active absorption method, are 7% smaller than with the passive method. Kristiansen and Faltinsen (2008) investigate wave loads on a constrained cylinder where a no-slip condition is imposed on the cylinder to consider fluid adhesion on the wall. No turbulence model is activated although the flow

can be turbulent and vortex structures form at the corner of the cylinder. The experimental and numerical loads show the same trend. However, the author notes that Morison's empirical formula cannot correctly predict the wave loads when overtopping occurs. In Chen et al. (2019), they model the interactions between a combined wave and current flow and a vertical surface piercing cylinder using a no-slip boundary condition. According to the authors, activation of a turbulence model is not necessary, especially because the loads are dominated by inertial effects (potential flow). A good agreement between the experimental and numerical results is obtained. Paulsen et al. (2014) perform a CFD test-bench with regular and irregular waves on a surface piercing structure. They do not consider the viscous layer imposing a zero velocity gradient on the cylinder, explaining that the flow is mainly inertial and the viscous effects are negligible as Chen et al. (2019). In all cases, the loads calculated with CFD successfully reproduce the experiments.

Several studies have been carried out using loads calculated with CFD models in the case of a cylinder subjected to waves. They include analysis of wave loads, comparison with the analytical formula and derivation of hydrodynamic coefficients. Paulsen (2013) demonstrates the dependence on water depth, wave height, and structure diameter of wave loads on a circular cylinder piercing the free surface for intermediate water depths. Paulsen compares the numerical loads to theoretical formulas such as Morison's empirical formula and third-order perturbation theories to predict ringing, as presented by Faltinsen et al. (1995) and Malenica and Molin (1995). In particular, he verifies the validity of these theories, originally developed for waves of low steepness, when extended to steeper waves. He also studies the impact of the wave on the cylinder, focusing on the creation of a secondary load cycle, a phenomenon that has already been discussed in Chaplin et al. (1997), Grue (2002), Rainey (2007). Yan et al. (2020) simulate the interaction of waves with a cylindrical payload using the solver `waveFoam`. They compare the numerical wave loads to the Morison force, without detailing the calculation of the coefficients that are considered ($C_D = 1$ and $C_M = 1.15$). Morison's approach correctly predicts the in-line force for each pitch angle tested, however, when testing different roll angles, Morison's prediction differs from the CFD results and another set of coefficients should be proposed for the different roll angles. They also focus on the influence of payload size and wave parameters on the wave loads. For these tests, no comparison with Morison's approach was performed. Bozonnet et al. (2015) model a heave plate in forced oscillations in OpenFOAM, in order to determine Morison coefficients from CFD results for this type of device, commonly used on FOWT systems. Benitz (2016) model the slanted member of a semi-submersible floater crossing the interface in different orientations and in a constant current (no wave). The cylinder was divided into slices to determine the loads on each slice. In this way, the author analysed the variation of the inline force along the length of the cylinder. Benitz (2016) also derive a frictional drag coefficient and a hydrostatic-free drag coefficient (i.e., omitting the hydrostatic pressure in the derivation) for each slice. To the author's knowledge, this is the only CFD study that sliced a cylinder along its axis to derive Morison coefficients. However, no waves were modelled, which would have complicated the derivation of coefficients.

In this paper, as a first step in the investigation of the hydrodynamics of floating wind turbines with a focus

on Morison formulation, the simple case of a fixed vertical cylinder in waves is considered using a Numerical Wave Tank implemented in the open-source CFD tool OpenFOAM. The NWT model, with waves only and then with the cylinder included, is validated against experiments. In this study, a set of dimensionless mesh features and numerical parameters are defined to obtain an appropriate CFD model. A comparison between the CFD results and the Morison approach is conducted. To derive comparable Morison loads, the so-called slice methodology is proposed to determine the Morison coefficients: instead of using the total load on the cylinder, the structure is sliced along its axis to derive Morison coefficients locally along the cylinder length. The proposed methodology is similar to standard methodologies for deriving coefficients from experimental loads, but it benefits from the information on local loads that is available in CFD and not in standard experiments. To illustrate the interest of such a method, the impact of the water depth and the interface on the loads and on the Morison coefficients is studied.

2. Material and Methods

2.1. Physical case study description

The surface-piercing cylinder CFD model is validated against experiments conducted by Stansberg (1997) at the MARINTEK wave tank facility. During this test campaign, regular and irregular deep-water waves propagated along a basin (10 m x 80 m) and interacted with cylinders of different diameters. These tests were extensively modelled in the IEA Wind OC5 project, where different engineering numerical tools were compared (Robertson et al. (2015)). Only a test of a regular wave interacting with a fixed vertical cylinder is selected for the present study. The cylinder is located 38.6 m from the wave paddles and its diameter is D = 0.2 m. The reported wave characteristics are: height H of 0.33 m, period T of 1.53 s, and water depth h of 10 m. According to Le Méhauté (1976), this wave can be classified as a deep-water and 3$^{\text{rd}}$ order Stokes wave.

Stokes 3$^{\text{rd}}$ order free surface elevation and velocity components in the horizontal and vertical directions are respectively formulated in Eq. 1, Eq. 2 and Eq. 3:

$$\eta(x,t) = (1 - \frac{3}{8}A^2k^2)A\cos\theta + \frac{1}{2}A^2k\cos(2\theta) + \frac{3}{8}A^3k^2\cos 3\theta, \tag{1}$$

$$u(x,z,\theta) = \frac{Agk'}{\omega}\exp(k'z)\cos(\theta), \tag{2}$$

$$w(x,z,\theta) = \frac{Agk'}{\omega}\exp(k'z)\sin(\theta), \tag{3}$$

where $\theta = (k'x - \omega t)$ and $k' = (1 - A^2k^2)k$. ω stands for the wave pulsation, k for the wave number and A for the wave amplitude, equal to $H/2$.

Accordingly, the corresponding location in Chakrabarti's wave load classification (Chakrabarti (2005)) shows that Morison's formulation should correctly predict the loads on the cylinder, with a small drag contribution and a large inertia term.

To classify the flow and load regime, two dimensionless numbers are introduced. The Keulegan-Carpenter number, that relates the amplitude of the oscillation to the diameter of the cylinder (Keulegan et al. (1958)), is defined by Eq. 4:

$$KC = \frac{u_m * T}{D} \ , \tag{4}$$

with u_m is the maximum velocity of the flow.

The Reynolds number is determined according to the recommendations of Massie and Journée (2001) for this type of configuration:

$$Re = \frac{\omega \frac{H}{2} D}{\nu} \ , \tag{5}$$

where ν is the kinematic viscosity of water.

For this case, $KC = 5.2$ and $Re = 1.4 \times 10^5$. The flow is thus considered as turbulent. For these values of KC and Re, the Morison formulation is appropriate to determine the wave loads.

In the experiments, the data measured are the elevation of the free surface at the centre of the cylinder when the cylinder is not present, and the forces and moments applied to the cylinder. The cylinder is attached at its top to a rigid frame. Two force transducers T1 and T2, visible in Fig. 1, record the loads along the direction of wave propagation.

2.2. CFD numerical model

To model wave-structure interactions, a NWT is implemented in OpenFOAM v1812 (Greenshields (2020)). The NWT is a fluid domain in which waves are generated at the inlet, propagate along the tank and are absorbed at the outlet, as shown in Fig. 2.

2.2.1. Governing equations and boundary conditions

The governing equations for an incompressible fluid are the continuity and momentum equations expressed as follows:

$$\nabla \cdot \mathbf{u} = 0 \ , \tag{6}$$

$$\frac{\partial(\rho \mathbf{u})}{\partial t} + \rho \nabla \mathbf{u} \cdot \mathbf{u} = -\nabla p^* + \nabla \cdot (\mu \nabla \mathbf{u}) + \rho \mathbf{g} \ , \tag{7}$$

where ∇ is the three-dimensional gradient operator, $\mathbf{u}$ the velocity field in Cartesian coordinates, $\mathbf{x}$ the position vector, p^* the pressure in excess of the hydrostatic pressure defined as $p^* = p - \rho \mathbf{g} \cdot \mathbf{x}$ (where p is the total pressure) and g the standard acceleration due to gravity. ρ is the fluid density, and μ is the dynamic viscosity, both defined as a function of the phase fraction α, (1 in water-filled cells, 0 in air), as follows:

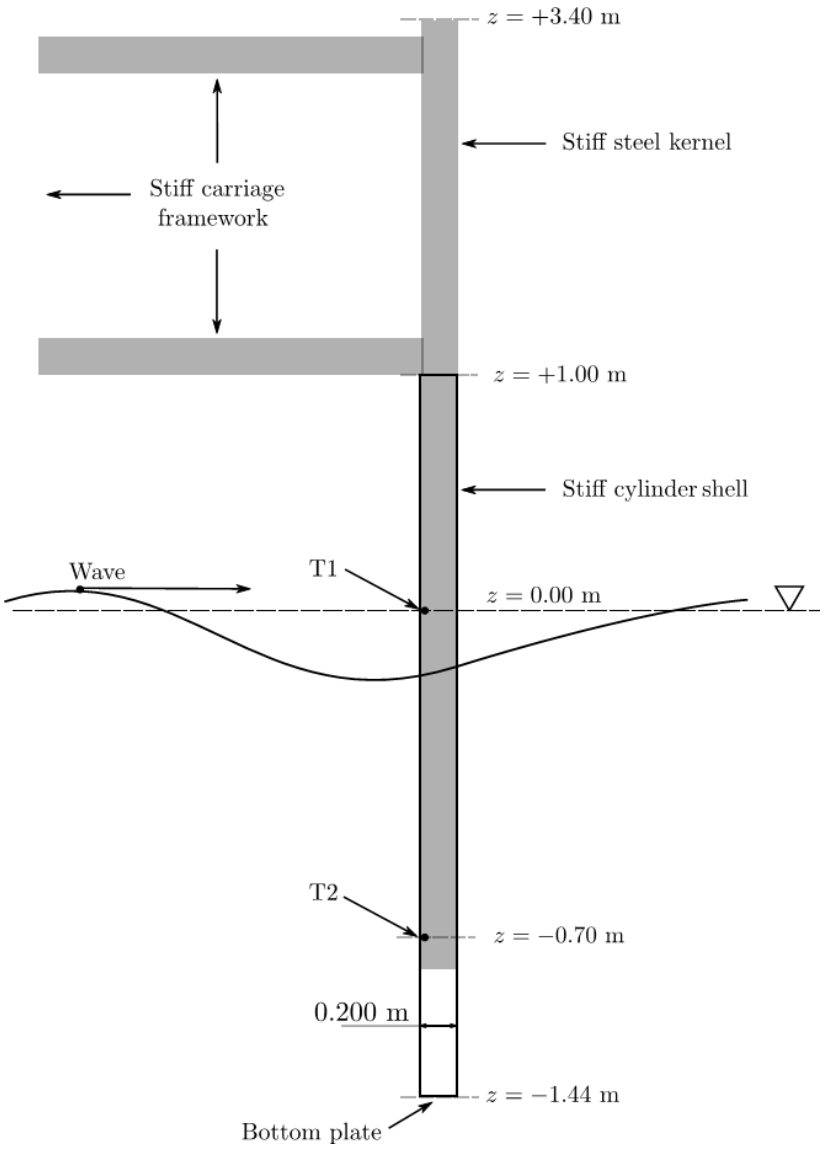

Figure 1: Cylinder test configuration from Stansberg (1997).

$$\rho = \alpha\rho_{water} + (1-\alpha)\rho_{air} \ , \tag{8}$$

$$\mu = \alpha\mu_{water} + (1-\alpha)\mu_{air} \ . \tag{9}$$

To track the air/water interface and to determine the phase fraction α, a Volume of Fluid (VOF) method is used, where α is governed by the following transport equation Eq. 10:

$$\frac{\partial\alpha}{\partial t} + \nabla\cdot(\alpha\mathbf{u}) + \nabla\cdot\mathbf{u}_c\alpha(1-\alpha) = 0 \ . \tag{10}$$

where $\mathbf{u}_c = \min(|\mathbf{u}|, \max(|\mathbf{u}|))\frac{\nabla\alpha}{|\nabla\alpha|}$.

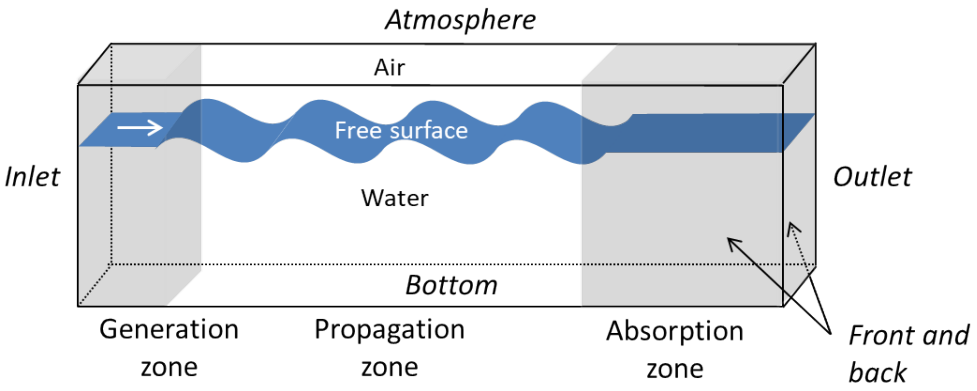

Figure 2: Numerical Wave Tank schematic. The cylinder will be included in the propagation zone.

The last term, specific to the VOF Multidimensional Universal Limited for Explicit Solution (MULES) method, is an artificial interface compression term to ensure the solution of the equation is bounded and to keep the interface sharp, as detailed by Weller (2008).

The waves2Foam library, implemented by Jacobsen (2017) is used to generate and absorb the waves. This passive method requires a relaxation zone at the entrance and exit of the domain, as shown in Fig. 2. The generation zone at the entrance is responsible for creating the waves and the absorption zone at the exit controls the damping of the waves to avoid reflection. In the generation and absorption zone, the velocity and alpha fields are updated at each time step based on a weighted function, χ, as shown in Fig. 3 and according to the following formula:

$$\mathbf{u} = \chi \mathbf{u}_{\mathbf{computed}} + (1 - \chi)\mathbf{u}_{\mathbf{target}} \ , \tag{11}$$

$$\alpha = \chi \alpha_{computed} + (1 - \chi)\alpha_{target} \ , \tag{12}$$

where $\mathbf{u}_{\mathbf{target}}$ and α_{target} represent the target values of the velocity and alpha fields, respectively. At the inlet, velocity and position of the interface are defined using a chosen wave theory. At the outlet, zero velocity and a free surface at rest are imposed. The calculated values ($\mathbf{u}_{\mathbf{computed}}$ and $\alpha_{computed}$) are the numerical values based on the solution of the Navier-Stokes and VOF equations.

Three weighted functions, χ, are available as explained by Jacobsen (2017). The most common is the default and the one used in this study, namely the weighted exponential function defined as:

$$\chi(\xi) = 1 - \frac{\exp\left(\xi^{\beta}\right) - 1}{\exp\left(1\right) - 1} \ , \tag{13}$$

where ξ represents the local coordinate system for the relaxation zones, the exponent β is set to 3.5 by default. The parameter χ is assigned in such a way that the target value ($\mathbf{u}_{\mathbf{target}}$ or α_{target}) gains more weight near

the boundary wall (inlet or outlet) and far from the propagation zone. Thus, the calculated field between the two relaxation zones is not affected by the boundary conditions of the input and output walls.

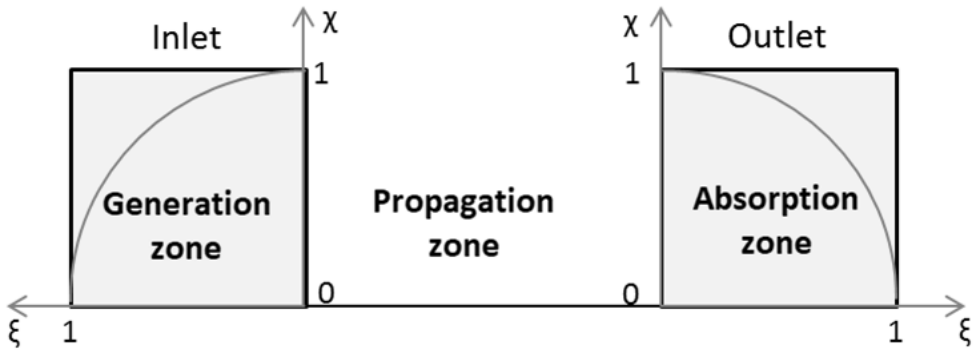

Figure 3: Relaxation zones.

The boundary conditions (BC) are imposed for the different fields (α, $\mathbf{u}$ and $p*$), at the tank boundaries (as shown in Fig. 2) and at the cylinder wall:

- Inlet: α and $\mathbf{u}$ are imposed according to the wave theory applied by the solver waveFoam. A null-gradient BC is imposed for $p*$.
- Outlet: the velocity is fixed at 0 and a null gradient is imposed for α and $p*$.
- Front and Back: a slip BC is imposed for $\mathbf{u}$, and a null gradient is imposed for $p*$ and α to avoid side effects.
- Atmosphere: the total pressure is fixed at 0. For $\mathbf{u}$, a zero gradient for the outflow velocity and a zero tangential component for the inflow velocity are imposed. A zero-gradient BC for α is imposed. Only air can flow back into the domain.
- Bottom: a zero gradient for α and $p*$ and a null velocity are imposed.
- Cylinder: in this study, two boundary conditions are tested; a slip BC (zero gradient for α and $p*$ and zero gradient for the normal component of the velocity) and a no-slip BC (zero-gradient for α and $p*$ and a zero velocity).

The 2^{nd} and 5^{th} order Stokes theories are implemented in the waves2Foam library and can be imposed at the inlet. In the present study, since the modelled wave can be classified as a 3^{rd} order Stokes wave, it is necessary to use the fifth-order boundary condition at the domain entrance.

Turbulence can be included using Reynolds Averaged Navier-Stokes (RANS) models, such as the k-omega SST model commonly used for offshore applications. However, this model induces a strong damping of the wave elevation, as noted by Larsen and Fuhrman (2018) who proposed a modified version, k-omega SST

stabRAS, more suitable for the resolution of the air/water interface. As pointed out in the literature review in the Section 1, a common practice is not to use any turbulence model, either with a slip or no-slip boundary condition on the structure wall. This seems to lead to a good agreement with the experimental results. These various options are tested in the present study, as presented in Section 4.1.3.

2.2.2. Numerical Wave Tank set up

It is crucial to ensure the accuracy and robustness of the CFD results before focusing on the physical analysis. This part dealing with the implementation of the numerical wave tank and its validation is described in great detail in Clément et al. (2020). The main results are summarised below, the reader is referred to this paper for more details.

Numerous simulations have been performed to verify the influence on the wave elevation of the mesh and domain characteristics (mesh refinement, length of the relaxation zones), of the time step and of the numerical parameters (spatial schemes, boundary conditions). To analyse the results, the wave elevation calculated at the cylinder location, but without the cylinder included, was compared to the experimental elevation. The reflection and damping of the waves were also studied by plotting the variation of the wave height along the tank.

Based on these numerical tests, a set of optimal parameters was determined to propagate the waves in a controlled manner while keeping the computation time reasonable; for example, running 140s of physical time in a case of 12M cells takes less than 2 days using 6 Intel Skylake G-6140 CPUs (each CPU consists of 18 cores running at 2.30GHz), i.e. 108 cores in total. A generation zone length of $1.2L$, L being the wavelength, allows for correct wave generation. The refinement along the vertical axis of the free surface area must be at least $H/12$, with H the wave height. This zone is centred around the mean sea level (MSL) and a height equal to $2H$ is recommended. During the time step convergence study, a large damping of the wave elevation along the NWT was detected for the largest time step ($T/300$). This behaviour can be related to the high air velocities observed on the wave crests, a limitation of the VOF method already highlighted by Afshar (2010), Paterson (2008) and Larsen et al. (2019). By decreasing the time step, these high air velocities are divided by 2 and the wave elevation is no longer damped. In addition, it can be seen that the smaller the time step, the larger the wave reflection. To achieve convergence of the time step while avoiding wave reflection, a fixed time step of $T/800$ with an absorption zone of 6 wavelengths is recommended. With this setting, a maximum Courant number of 0.08-0.09 is obtained in the simulation, respecting the advice of Larsen et al. (2019) to aim at a maximum Courant number of 0.1 in the case of wave modelling with the VOF MULES method.

2.3. Post-processing quantities

The following statistics are applied to analyse the wave elevation time series or the wave load, both of which are represented in this paragraph by a function $f(t, x, y, z)$. The signals analysed in this study are periodic

and sinusoidal as shown in Fig. 4. The twenty last periods of the CFD and experimental signals are used to derive the statistics detailed below.

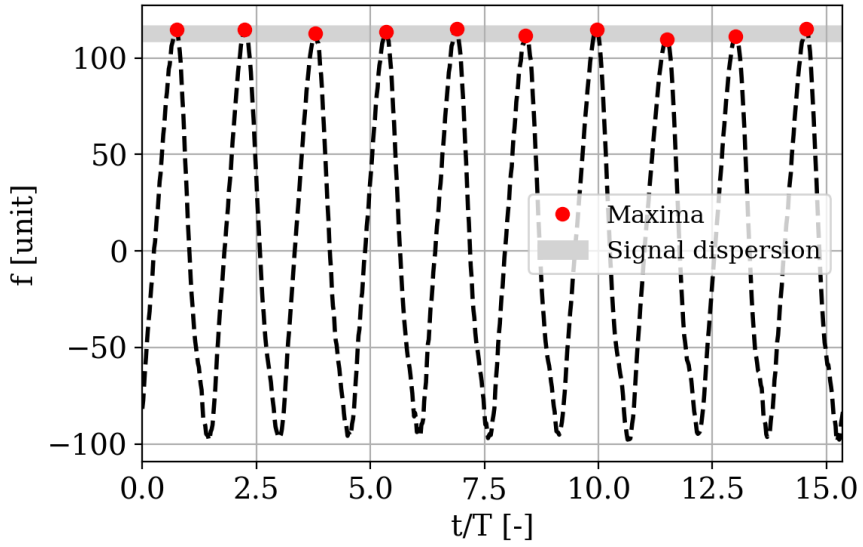

Figure 4: Example of an analysed signal.

Signal dispersion. The dispersion of the signal is determined by the standard deviation of the series of maxima of the time signal, σ_{max}. The signal is considered to be stabilised in time if the maxima evolve in a band of $\pm 2\sigma_{max}$ around the mean of the maxima (confidence interval of 95%), as represented by the grey band in Fig. 4. In this study, the dispersion is often presented in percentage via the following ratio (variation on the mean value):

$$Disp = \frac{2\sigma_{max}}{\frac{1}{n}\sum_{i=1}^{n} f_{max}(t_i, x, y, z)} \ , \tag{14}$$

where $f_{max}(t, x, y, z)$ is the series of the maxima of the time signal $f(t, x, y, z)$.

Signal height. In the global reference frame $(Oxyz)$, the signal height at a location (x,y,z) in the tank is determined from $f(t, x, y, z)$ as stated in (Eq. 15):

$$H_{calc}(x, y, z) = 2\sqrt{2\text{var}(f(t, x, y, z))} \ , \tag{15}$$

where

$$\text{var}(f(t, x, y, z)) = \frac{1}{n}\sum_{i=1}^{n}(f(t_i, x, y, z) - \bar{f}(x, y, z))^2 \ , \tag{16}$$

with $\bar{f}(x, y, z)$ the signal average over time.

Error quantification on signal height. To quantify the differences between the time signal derived from the CFD simulations and the reference (experimental or theoretical signal), the percentage error between the height derived from the two signals is determined as follows:

$$\text{Error}(H_{CFD}, H_{ref}) = \frac{H_{CFD} - H_{ref}}{H_{ref}} * 100 \ . \tag{17}$$

Error quantification on time series. The Normalised Root Mean Square Error (NRMSE), used to accurately compare two signals over time, is defined as in (Eq. 18):

$$\text{NRMSE} = \frac{\sqrt{(\frac{1}{n})\sum_{i=1}^{n}(f_{CFD}(t_i, x, y, z) - f_{ref}(t_i, x, y, z))^2}}{H_{ref}} \ , \tag{18}$$

where $f_{CFD}(t_i, x, y, z)$ is the time signal at time t_i derived from the CFD simulation and $f_{ref}(t_i, x, y, z)$ is derived from the experimental or theoretical model, and n the total number of time steps.

To complement these statistics, graphs against time are presented. The experimental wave elevation and load signals are rather scattered, as can be seen for the wave elevation in Fig. 5 for example.

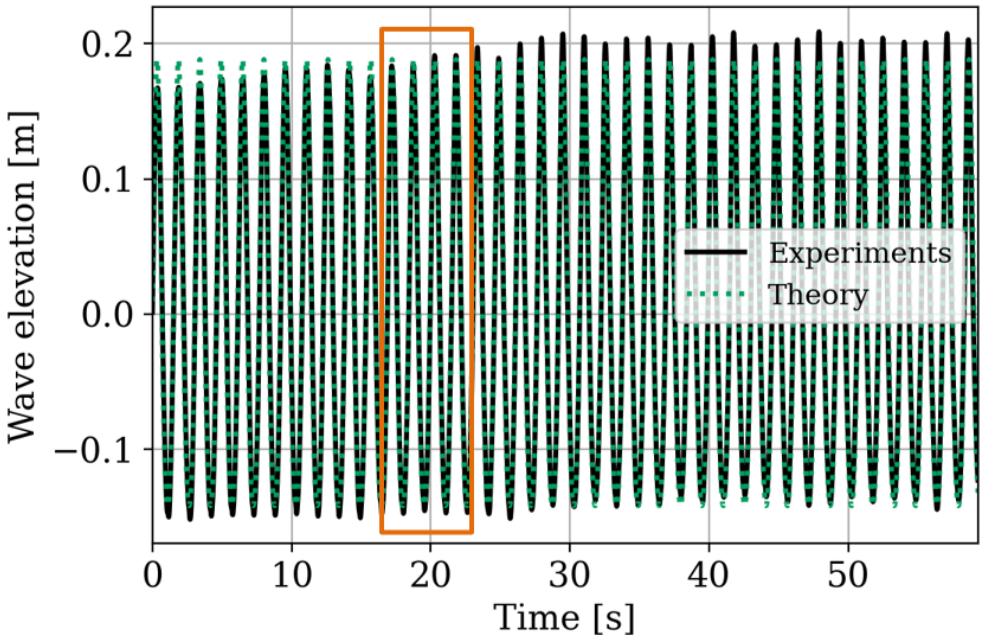

Figure 5: Wave elevation time series from Stansberg experiments.

To compare the shapes of the plots (amplitude, phase, peak and trough shape), the visualisation is limited to four periods. To obtain a fair comparison and because the experimental elevation is not stable, the starting time of this four-period zoom is chosen when the experimental elevation and the theoretical elevation (based on third-order wave theory) match sufficiently well, namely during the period represented in the rectangular area in Fig. 5.

After presenting the case under study, the experimental data, the numerical model and the specifics of the post-processing, the methodology to evaluate the Morison coefficients from the CFD loads, for the specific case of a vertical cylinder, is detailed in the next section.

3. Methodology to estimate Morison coefficients from CFD simulations

Stansberg cylinder being considered as a slender element ($D = 0.2m << \lambda = 3.65m$), Morison empirical formula can be applied to predict the wave loads on the structure.

3.1. Morison empirical formula

As Morison empirical formula is derived for an infinite cylinder, the theoretical expression is commonly reported per unit length of cylinder, and the total loads are obtained by integrating the expression over the cylinder.

As all components of the forces along the cylinder axis are assumed to be negligible, only the components of the flow and forces in the plane perpendicular to the cylinder axis are considered. In the case of the vertical cylinder considered in this study (Fig. 6), the axial forces are zero ($F_z = 0$) and the force has only two components along the axes (Ox) and (Oy): F_x and F_y.

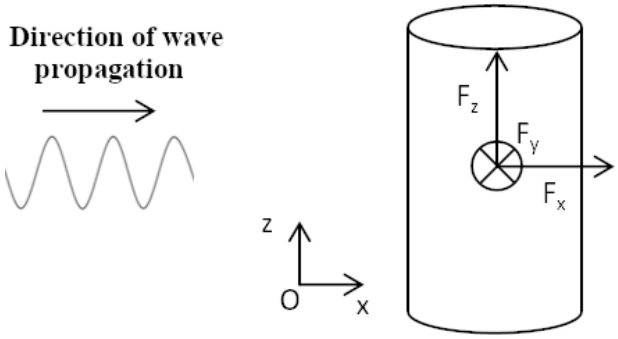

Figure 6: Vertical cylinder in waves.

Assuming that the wave propagates only along the (Ox) axis, F_y is also zero and the theoretical force has only one component F_x, expressed as :

$$F_x(z,t) = \frac{1}{2}\rho C_D D u(x,z,t)|u(x,z,t)| + \frac{\rho\pi D^2}{4} C_M \dot{u}(x,z,t) \ , \tag{19}$$

where $u(x,z,t)$ and $\dot{u}(x,z,t)$ are respectively the velocity and acceleration of the undisturbed wave, calculated at the centre of the cylinder and projected on the (Ox) axis, on the basis of theoretical models (Eq. 2). C_D and C_M are respectively Morison's drag and inertia coefficients.

3.2. Slice method for determining local Morison coefficients from CFD results

In the case of a vertical cylinder, the Morison force depends only on the z-coordinate and time (cf. Eq. 19). To take into account the water depth dependence, the cylinder is divided into slices along the (Oz) axis,

which makes this method innovative compared to experimental methods which are often limited to the total force measured on the whole cylinder (Chaplin and Subbiah (1997), Wolfram and Naghipour (1999)).
To determine the Morison coefficients from a CFD simulation of a cylinder subjected to waves, the following method is applied for each slice:

1. The load on the slice is extracted from the CFD simulation. Both pressure and viscous contributions are included in the calculated load, as described in Greenshields (2020). The CFD load time series are extracted over a time interval T_{int}, consisting of an exact number of periods, N_P; for this study, $N_P = 26$. For each period k ($k = [1 : N_P]$), I time values of each force component in the global reference frame ($Oxyz$) are output and defined as $F_{CFD}(t_i)$ where i is the time index ($i = [0 : I]$).
2. The wave velocity and acceleration ($u(z, t_i)$ and $\dot{u}(z, t_i)$ respectively) are determined at the centre of the slice. The time series are then obtained using Stokes 3$^{\text{rd}}$ order theory (Eq. 2) rather than CFD results. This point is discussed in more detail in section 4.1.2.
3. For each period k of T_{int}, the hydrodynamic coefficients C_D^k, C_M^k are calculated following the steps detailed below:
   (a) The error $R^{k,2}$ between the CFD loads $F_{CFD}(t_i)$ and those based on Morison theoretical expression $F_{Mor}(t_i)$ (Eq.19) is determined as follows:

$$R^{k,2} = \sum_{i=1}^{I} [F_{Mor}(t_i) - F_{CFD}(t_i)]^2 \tag{20}$$

$$R^{k,2} = \sum_{i=1}^{I} [\frac{1}{2}\rho C_D^k D u(z, t_i)|u(z, t_i)| + \frac{\rho\pi D^2}{4} C_m^k \dot{u}(z, t_i) - F_{CFD}(t_i)]^2 \tag{21}$$

$$R^{k,2} = \sum_{i=1}^{I} [f_D^k u(z, t_i)|u(z, t_i)| + f_I^k \dot{u}(z, t_i) - F_{CFD}(t_i)]^2 \tag{22}$$

   where $f_D = \frac{1}{2}\rho D C_D^k$ and $f_I = \frac{\rho\pi D^2}{4} C_M^k$
   (b) The error $R^{k,2}$ is minimised by cancelling its derivative as a function of drag and inertia terms (f_D^k and f_I^k respectively) as explained in Sumer et al. (2006) and detailed below:

$$\begin{cases} \dfrac{\partial R^{k,2}}{\partial f_D} = 0 \\ \\ \dfrac{\partial R^{k,2}}{\partial f_I} = 0 \end{cases} \tag{23}$$

   (c) The two-equation system of Eq. 23 is then solved to obtain the drag and inertia Morison coefficients for a given period k.

$$C_D^k = \frac{2}{\rho D} \frac{\sum_{i=1}^{I} F_{CFD} u(z,t_i)|u(z,t_i)| \sum_{i=1}^{I} \dot{u}^2(z,t_i) - \sum_{i=1}^{I} F_{CFD} \dot{u}(z,t_i) \sum_{i=1}^{I} u(z,t_i)|u(z,t_i)|\dot{u}(z,t_i)}{\sum_{i=1}^{I} u^4(z,t_i) \sum_{i=1}^{I} \dot{u}^2(z,t_i) - (\sum_{i=1}^{I} u(z,t_i)|u(z,t_i)|\dot{u}(z,t_i))^2} \tag{24}$$

$$C_M^k = \frac{4}{\rho \pi D^2} \frac{\sum_{i=1}^{I} F_{CFD} \dot{u}(z,t_i) \sum_{i=1}^{I} u^4(z,t_i) - \sum_{i=1}^{I} F_{CFD} u(z,t_i)|u(z,t_i)| \sum_{i=1}^{I} u(z,t_i)|u(z,t_i)|\dot{u}(z,t_i)}{\sum_{i=1}^{I} \dot{u}^2(z,t_i) \sum_{i=1}^{I} u^4(z,t_i) - (\sum_{i=1}^{I} u(z,t_i)|u(z,t_i)|\dot{u}(z,t_i))^2} \tag{25}$$

where F_{CFD} is provided by step 1 of the methodology, and $u(z,t_i)$ and $\dot{u}(z,t_i)$ are calculated in step 2. The expressions of drag and inertia coefficients given by Eq. 24 and Eq. 25 correspond to those obtained for experimental data for a vertical cylinder by Wolfram and Naghipour (1999).

4. To eliminate any temporal variation in the numerical loads, the drag and inertia coefficients are averaged over the N_P periods. The time-averaged Morison coefficients C_D and C_M are then defined as follows:

$$\begin{aligned} C_D &= \sum_{k=1}^{N_P} C_D^k, \\ C_M &= \sum_{k=1}^{N_P} C_M^k. \end{aligned} \tag{26}$$

Finally, by applying the above procedure to each slice of the cylinder, a set of Morison coefficients C_D and C_M is obtained for each slice along the cylinder.

In the following results section, this methodology is applied to the vertical cylinder case study to derive the Morison hydrodynamic coefficients. The Morison loads are then compared to original CFD loads and the differences are discussed.

4. Results

This section is composed of three subsections. The first presents the validation of the CFD simulations against experiments. The second subsection deals with the application of the slice method detailed in section 3.2 to the case of the vertical cylinder: first, the hydrodynamic coefficients are determined and then the resulting loads on each slice and on the whole cylinder are successively analysed. The third subsection presents a physical analysis of the influence of the interface on the wave loads.

4.1. Validation and presentation of CFD results

In this section, the final results obtained with the Numerical Wave Tank configuration detailed in subsection 2.2.2 are presented.

4.1.1. Wave only case - wave elevation

The wave elevations at the centre of the tank without the cylinder obtained numerically, experimentally and theoretically (3rd order Stokes theory) are compared in Fig. 7. It shows that all three signals have very similar period and amplitude, demonstrating the ability of the CFD model, defined as advised in section 2.2.2, to reproduce the experimental wave elevation at a given location in the tank.

The NRMSE of the theory compared to the experiments is 2.9%. Taking into account the dispersion of the experiment ($Disp$ = 13%, see Fig. 5), the theoretical formula reproduces the experiments quite well. The NRMSE of the CFD compared to the experiments is 3.3%. Thus, the CFD, theoretical and experimental time series of wave elevation at the centre of the tank are in excellent agreement.

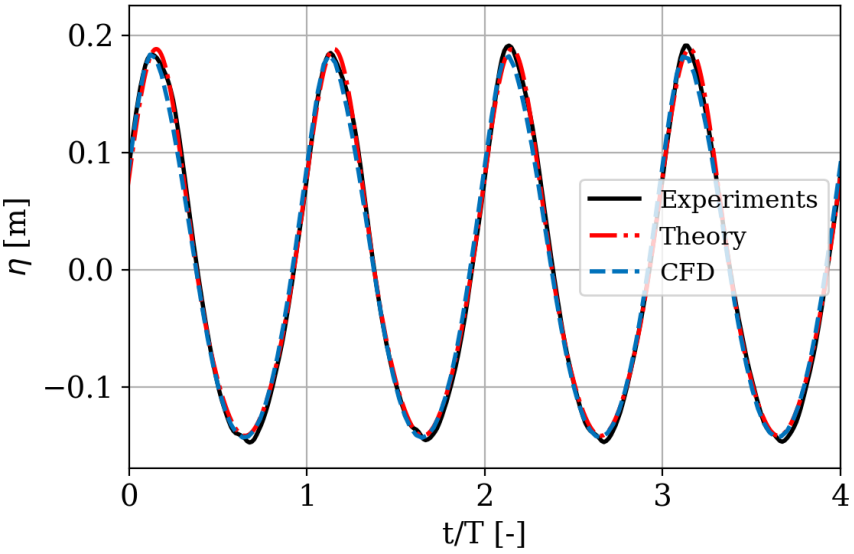

Figure 7: Wave elevation time series at the centre of the tank. Experimental data from Stansberg (1997).

The variation of the wave height along the tank plotted in Fig. 8 shows a very small variation of the amplitude along the tank and remains close to the theoretical value. The damping and reflection along the NWT are considered negligible.

4.1.2. Wave only case - velocity profile

The CFD velocity profile is determined from the time series of the wave velocity at the cell centres on a vertical line, where the cylinder will then be located.

The theoretical velocity below the Mean Sea Level (MSL) is based on the 3rd order Stokes wave theory (cf. Eq. 2). A specific treatment is performed on the theoretical velocity for $z > MSL$ to take into account the variation of the sea level with time. Indeed, a so-called stretching model is used to extrapolate the velocity profile between the MSL and the maximum wave elevation A_{max}. Different stretching methods are tested and compared in Fig. 9:

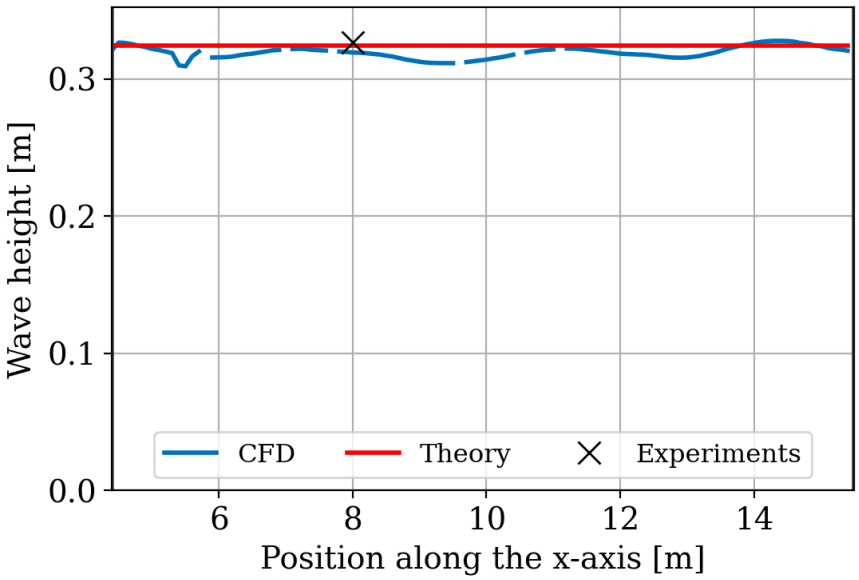

Figure 8: Wave height variation along the tank. Experimental data from Stansberg (1997).

- The vertical stretching model keeps the velocity constant and equal to the velocity at the MSL (orange dashed curve in Fig. 9).
- Wheeler stretching model consists of stretching the vertical scale (dark blue dotted curve in Fig. 9). Wheeler et al. (1970) propose to take the velocity/acceleration of the wave at $z = \eta$ (η the wave elevation) equal to the velocity given by the theory at $z = MSL$. z is then changed into z' as in Eq. 27 (where h is the water depth):

$$z' + h = h(\frac{z+h}{h+\eta}) \ . \tag{27}$$

- The extrapolated stretching model simply consists in extrapolating the 3$^{\text{rd}}$ order Stokes formula (Eq. 2) for $z > MSL$ (green dashed curve in Fig. 9).

Fig. 9 shows the profiles determined from the maximum of the CFD and theoretical velocity time series. The theoretical interface zone, which lies between A_{max} and A_{min}, is also shown on the graph.
For the water depths below the MSL, 3$^{\text{rd}}$ order Stokes wave theory (red dashed curve) and CFD (solid blue curve) are in good agreement, whereas Wheeler stretching model leads to lower velocities.
Another major difference lies in the prediction of the velocity near the wave crest (A_{max}). The CFD seems to overestimate the maximum velocity compared to Stokes wave theory combined with any of the stretching models. This is also highlighted by Larsen et al. (2019) who demonstrates that velocities at the wave crests are very often overestimated with VOF methods. Wheeler stretching model strongly underestimates the velocity in the interface zone. Between MSL and A_{max}, as the extrapolated stretch model best predicts the CFD profile, the 3$^{\text{rd}}$ order Stokes wave theory combined with the extrapolated stretch model is chosen as the theoretical reference model.

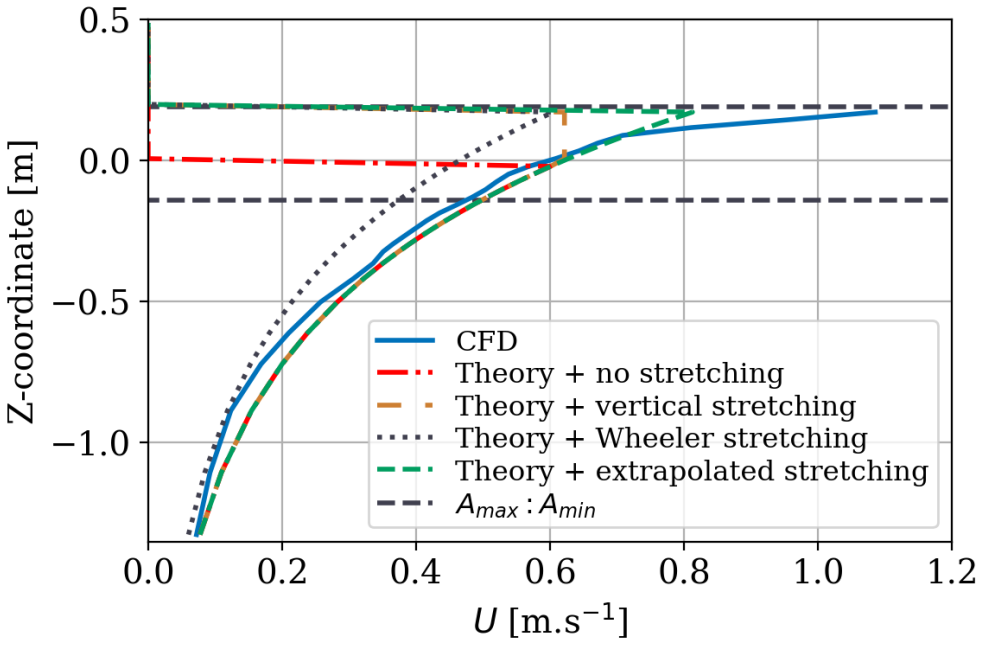

Figure 9: Velocity profile along water depth.

To complete this comparison, the dispersion of the CFD velocity profile, defined as a band of width $\pm 2\sigma_{max}$ around the average of maxima, is plotted in Fig. 10. It shows that the theoretical velocity profile is always contained within the dispersion band around the CFD profile, except for the very upper part of the interface area. This agreement on the velocity profiles between CFD and wave theory with extrapolated stretching method concludes the validation of the wave-only NWT model.

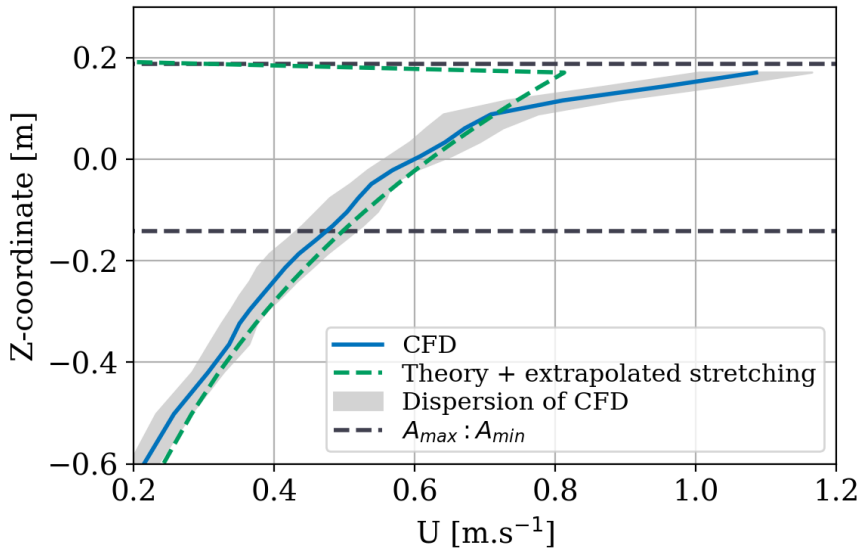

Figure 10: Velocity profile along water depth (zoom).

To derive the Morison coefficients for each slice by applying the numerical slice method (see section 3.2), the time series of undisturbed velocities at the centre of each slice is required; from the above results, the Stokes 3rd order theory combined with an extrapolated stretching model in the Morison formula is chosen.

4.1.3. Wave loads

The robustness and validity of the wave-only NWT has been assessed and the cylinder is now included in the NWT.

As detailed in section 1, a clear consensus is not identified in the literature on the boundary conditions that should be applied on the cylinder wall for the velocity/pressure fields. For this reason, three tests are performed and their impact on the forces is analysed.

A slip Boundary Condition (BC) on the cylinder (zero velocity gradient) is compared to a no-slip BC (zero velocity), both tests are performed without a turbulence model. An additional level of refinement is imposed around the cylinder in order to obtain cells of size D/15 near the structure. The third CFD simulation is performed by activating the k-omegaSST stabRAS turbulence model with the no-slip BC developed by Larsen et al. (2019). The mesh refinement near the cylinder satisfies the requirements of the wall functions ($30 < y+ < 300$, with $y+$ the non-dimensional wall distance).

Fig. 11 compares the horizontal force over four periods for the three tests detailed above. The CFD loads are slightly underestimated compared to the experiments. For the three CFD cases, the difference with the experiments is less than 8%, which is comparable to the dispersion of the experimental signal ($Disp = 7\%$). Furthermore, the peak-to-peak magnitude and the small bump before the minimum are well predicted by all simulation setups. These results imply that the turbulence model is not necessary in this case.

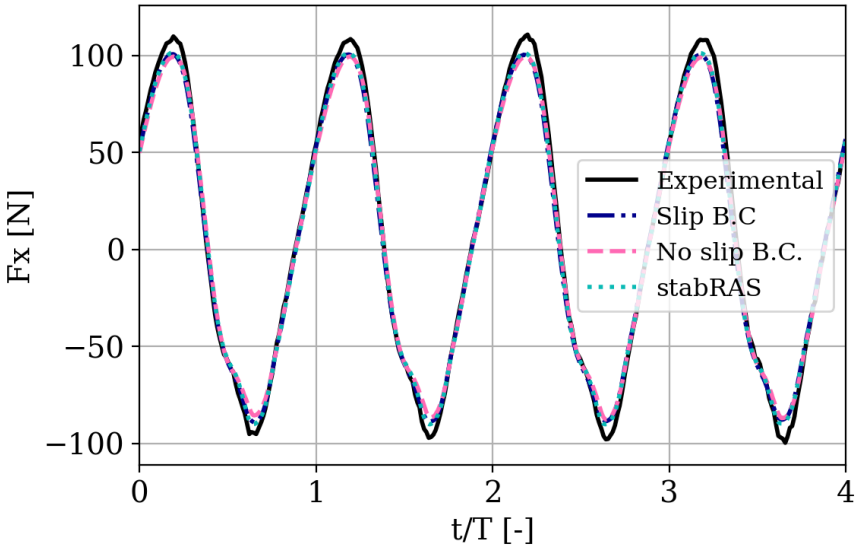

Figure 11: Horizontal wave loads (F_x) on the fixed cylinder. Experimental data from Stansberg (1997).

Finally, a no-slip BC is imposed on the cylinder wall and no turbulence model is activated. The statistics

obtained with this CFD model are presented in Tab.1.

Case	F_x [N]	Error(CFD, Expe) [%]	NRMSE(CFD, Expe) [%]
Experiments	198.2	/	/
CFD (no-slip BC)	183.4	-7.4%	4.1%

Table 1: Comparison between CFD and experimental horizontal wave loads (F_x).

With the NWT validated for the only-wave configuration and with the cylinder against the experimental data, the slice methodology is applied to derive the Morison coefficients from the CFD loads.

4.2. Application of the slice method

4.2.1. Determination of Morison coefficients

For each slice depicted in Fig.12, a set of Morison coefficients is derived from the inline CFD wave loads (F_x) by applying the slice methodology. The unperturbed velocity/acceleration time series at the centre of each slice are determined by applying 3$^{\text{rd}}$ order Stokes wave theory combined with an extrapolated stretching model as mentioned earlier. The size of the slices was set so that the velocity gradient was constant per slice; the size of the slices in the interface zone is therefore smaller, in agreement with the velocity profile (Fig. 9).

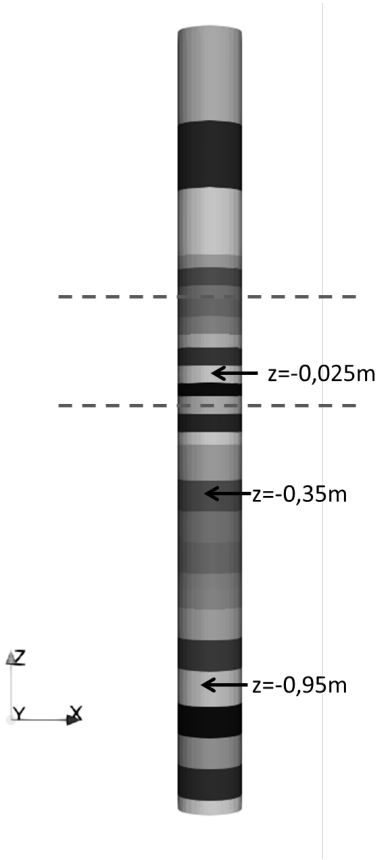

Figure 12: Sliced cylinder and location of the analysed cylinder slices.

The variation along the cylinder of C_M and C_D are shown in Fig. 13. The coefficient of inertia C_M increases slightly with z along the immersed part of the cylinder; the value of C_M averaged over the immersed part of the cylinder is 2.00 with a dispersion of ± 0.22 around the mean value. The results are consistent with values commonly defined in standards, such as DNV-RP-C205 Veritas (2010). In the OC5 project (Robertson et al. (2015)) where the same cylinder is modelled with design tools, the participants also obtained $C_M = 2$. This agreement confirms the validity of the CFD model and the implementation of the coefficient calculation.

In the region between A_{min} and A_{max}, the coefficient of inertia decreases sharply, probably because the Morison formulation is no longer applicable near the air/water interface, as will be seen later. Thus, the Morison coefficients derived from the CFD loads in the slices near the interface zone have a limited physical meaning.

In Fig. 13, the drag coefficient C_D varies greatly along the water depth, ranging from -1.37 to 1.51. Boccotti (2014) also obtained negative drag coefficients from the experimental loads on a cylinder for a Keulegan-Carpenter number KC lower than 5 (in the present case $KC = 5.2$). These values can also be explained by the negligible contribution of the drag load compared to the inertial force, which makes its calculation and, consequently, the determination of the drag coefficient unreliable. To illustrate this point, the time series of the total Morison load (using the mean hydrodynamic coefficients plotted in the Fig. 13), as well as its

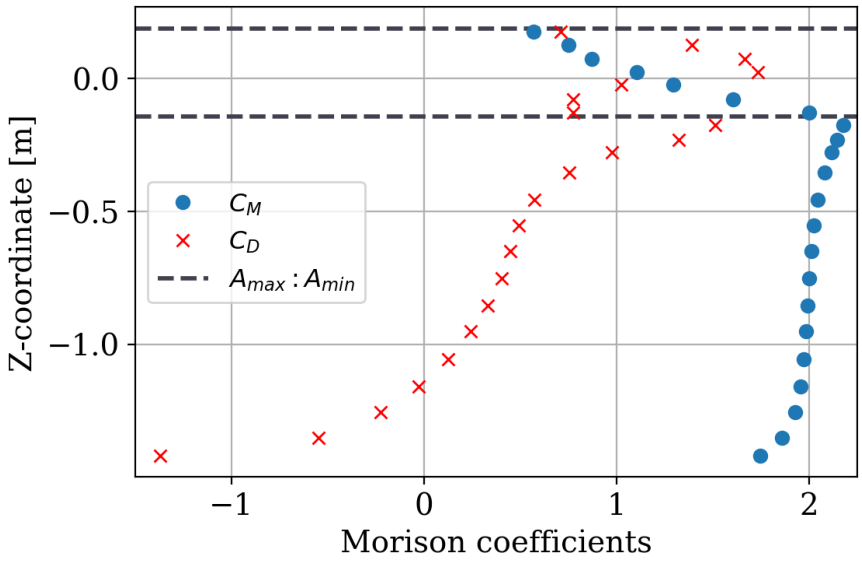

Figure 13: Morison inertia and drag coefficients for each slice.

contribution to drag and its contribution to inertia, are calculated and plotted in Fig. 14.

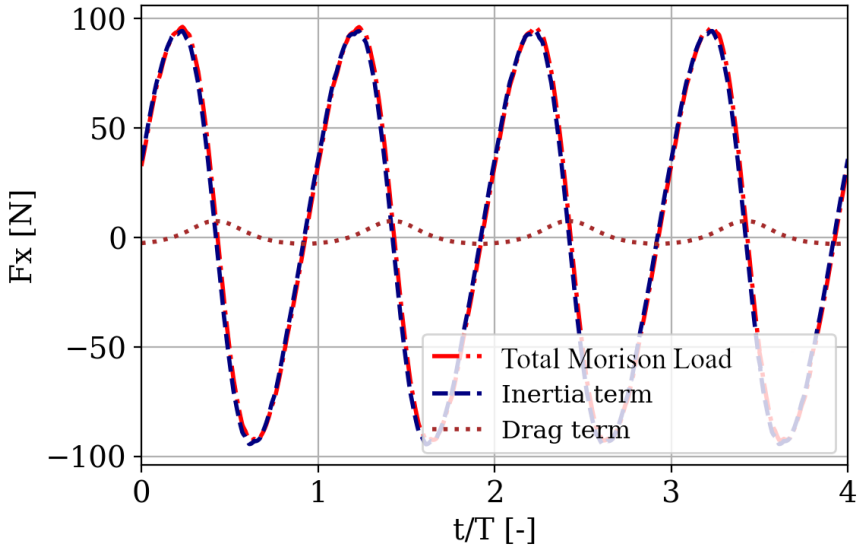

Figure 14: Morison loads on the cylinder: total load, inertia and drag contributions.

4.2.2. Analysis of CFD and Morison loads along the cylinder

The influence of the air/water interface on the loads and the limitation of Morison's theory to predict the loads for slices located in the interface zone are discussed below. To do so, the loads calculated from the CFD pressure field are compared with the loads derived from Morison's formulation, with the coefficients calculated from the CFD. Three slices centred at different water depths, $z = -0.95\,\mathrm{m}$, $z = -0.35\,\mathrm{m}$ and $z = -0.025\,\mathrm{m}$

are considered for analysis; the three slices are identified in Fig. 12. The hydrodynamic coefficients C_M and C_D, used to calculate the Morison force along the cylinder, can be determined in two different ways:

- Variable coefficients (denoted C_D, C_M (variable)): the coefficients derived for each slice are directly used in the calculation of the force.
- Averaged coefficients (denoted C_D, C_M (averaged)): the coefficients are averaged over all the immersed slices ($z < A_{min}$), and then used to calculate the force.

The Morison hydrodynamic coefficients determined with the two methods are listed in Tab. 2.

Coefficient	$z = -0.95\,\mathrm{m}$	$z = -0.35\,\mathrm{m}$	$z = -0.025\,\mathrm{m}$
C_D (variable)	0.24	0.76	1.02
C_D (averaged)	0.33	0.33	0.33
C_M (variable)	1.98	2.08	1.29
C_M (averaged)	2.00	2.00	2.00

Table 2: Morison coefficients determined from CFD with two different methods on three different slices.

For a slice deeply submerged, at $z = -0.95\,\mathrm{m}$

In Fig. 15, the CFD and Morison loads are plotted for the slice centred at $z = -0.95\,\mathrm{m}$, which is always immersed. The Morison formulation, regardless of the coefficient calculation method used (variable or average), leads to a prediction in excellent agreement with the reference loads provided by the CFD.

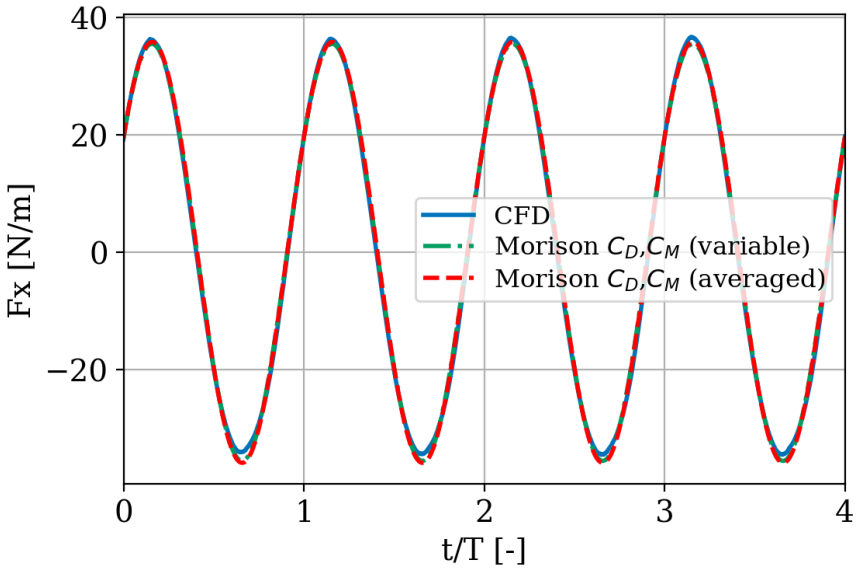

Figure 15: Comparison between CFD and Morison loads on the slice centred at $z = -0.95\,\mathrm{m}$.

For a slice below the interface zone, at $z = -0.35\,\mathrm{m}$

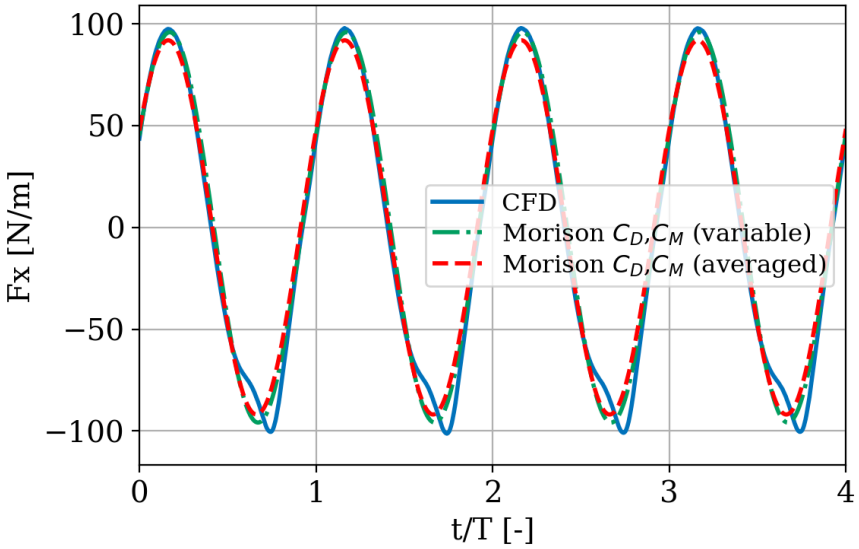

Figure 16: Comparison between CFD and Morison loads on the slice centred at $z = -0.35\,\mathrm{m}$

As shown in Fig. 16, for a slice centred at $z = -0.35\,\mathrm{m}$, closer to the interface but below $z = A_{min}$, a bump appears on the CFD force signal near the trough, which cannot be predicted with the Morison formulation. This bump, related to the influence of the interface, will be studied in more detail in section 5. Despite this slight difference, the variation and amplitude of the load are fairly well predicted by Morison formula, whatever the coefficient calculation method used.

For a slice within the interface zone, $z = -0.025\,\mathrm{m}$

CFD and Morison load predictions are compared in Fig. 17 for a slice centred at $z = -0.025\,\mathrm{m}$. The loads are zero as long as the slice is in the air. When the slice is submerged in water, the same behaviour is observed as for a slice close to the interface: the force increases then decreases. A hump occurs just before the trough, which is more pronounced than for the slices that are more deeply immersed.

This complex behaviour of the load is not well predicted by Morison's formulation, which was developed for a fully submerged cylinder and is therefore not suitable for a cylinder piercing the free surface. Regardless of the hydrodynamic coefficient calculation method, the sinusoidal shape of the Morison signal does not correctly reproduce the complex shape of the load on the slices close to the interface.

Load profile along the cylinder

Fig. 18 shows the force profiles along the cylinder, obtained by CFD and Morison theory with the variable and average coefficients. The force profile along the depth is calculated by applying the Eq. 15 on the force on each slice. The Morison load based on the variable method for calculating the hydrodynamic coefficient closely matches the CFD load. In the interface zone, significant differences are observed between the CFD load and

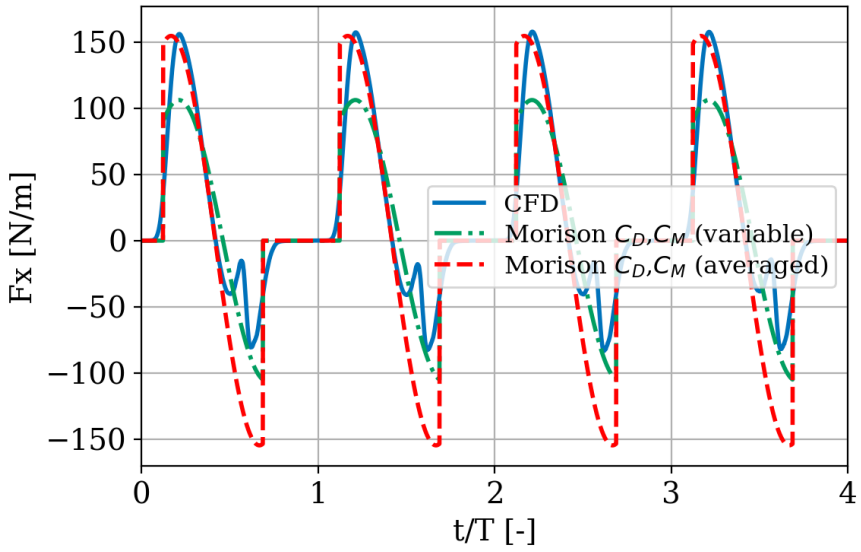

Figure 17: Comparison between CFD and Morison loads on the slice centred at $z = -0.025\,\mathrm{m}$

the Morison load calculated from average hydrodynamic coefficients, in agreement with the observations in Fig. 17.

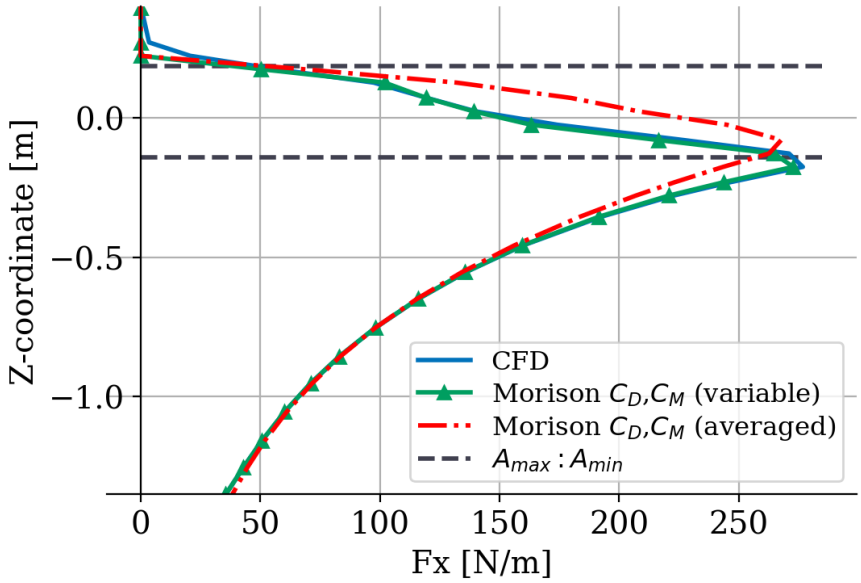

Figure 18: CFD and Morison force profiles along the cylinder length.

4.2.3. Analysis of the total CFD and Morison total loads on the whole cylinder

This subsection deals with the prediction of the total load on the cylinder. The Morison loads are obtained by summing the loads on each slice, using the variable and the average method for calculating the hydrodynamic coefficients.

In Fig. 19, the time series of total loads obtained from the CFD simulation, Morison formula and experiments are compared. It is first observed that all four signals have the same period. The small hump just before the trough, related to the air/water interface as explained in section 4.2.2, is visible on the experiments and well predicted by the CFD. Morison's formula with variable hydrodynamic coefficients predicts this non-linear effect better than the formula using average hydrodynamic coefficients as shown in Fig. 20. As explained in Section 4.2.2, using the variable method to calculate the hydrodynamic coefficient helps Morison's theory to better predict the loads in the air/water interface zone, though Morison's formulation is not suitable for such a configuration.

Nevertheless, the NRMSE between the CFD and Morison loads is 4.26% when using average coefficients and 4.16% when using variable coefficients. As the errors are relatively small for this case of a slender cylinder, it can be concluded that both methods are accurate enough to estimate the total load on the whole cylinder. These results also show that the coefficient and load determination must be performed with great care, especially when dealing with cylinders mainly located within the free surface area.

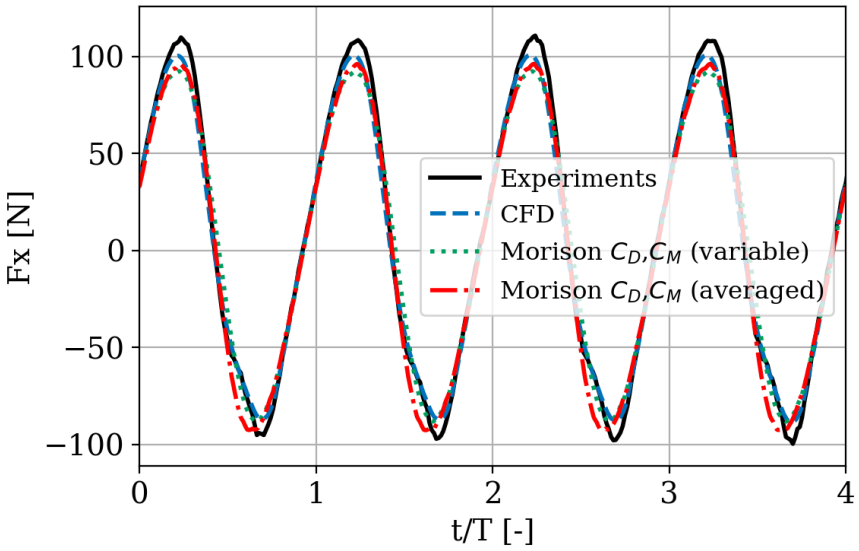

Figure 19: CFD, experimental (Stansberg (1997)) and Morison total loads on the cylinder.

5. Physical analysis of the influence of the interface on the wave loads

The influence of the interface on the wave loads for the surface-piercing cylinder is analysed in two steps in this section. First, the non-linear behaviour of the total inline force is studied, by comparing the CFD loads with those obtained in previous experimental and numerical studies. Then, the correlation between the wave loads and the interface behaviour is investigated using the CFD simulation results.

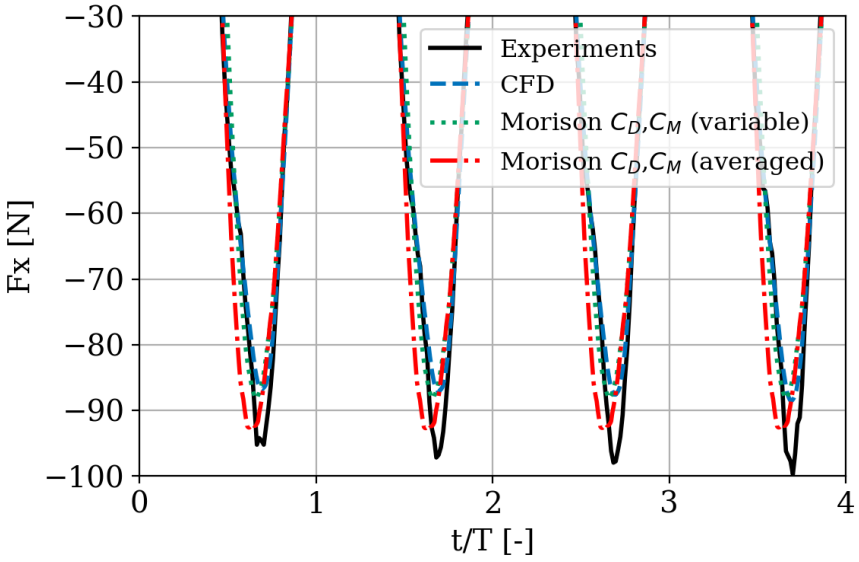

Figure 20: CFD, experimental (Stansberg (1997)) and Morison loads on the cylinder (zoom).

5.1. Non-linear diffraction load on the surface-piercing cylinder

The non-linear effect, characterised by a bump before each minimum on the wave load graph in Fig. 19, has already been studied numerically and experimentally. Indeed, Paulsen et al. (2014) examined numerically the forces exerted on a bottom fixed circular cylinder by steep regular waves at finite water depth. The authors observe the appearance of an additional local peak at the time of the minimum load, known as the secondary load cycle.

Ferrant (1998) describes the non-linear interaction between a regular wave and a surface-piercing cylinder by performing simulations with ANSWAVE, a fully non-linear Boundary Element Model. He reveals the existence of short diffraction waves around the cylinder which can trigger ringing, a potentially dangerous non-linear excitation for an elastic structure, with burst-like characteristics precisely described by Chaplin et al. (1997).

Huseby and Grue (2000) experimentally studied the first and higher harmonic components of wave loads on a vertical cylinder. A large set of waves with slopes (kA) up to 0.24 was tested. Ferrant (1998) numerically modelled the Huseby and Grue (2000) experiments for slopes up to 0.145 ($kR = 0.245$). Good agreement between the numerical and experimental models is obtained for the 3^{rd} to the 5^{th} harmonics but significant differences exist for the 2^{nd} harmonic. Overall, the force decreases as the slope of the wave kA becomes larger.

The characteristics of the Stansberg wave/cylinder case are $kR = 0.17$, $kh = 17$, $kA = 0.28$. In Tab.3 the amplitudes of the first five harmonics of the wave loads are provided for the Stansberg experiments and the present CFD model. The amplitude is made non-dimensional by dividing the n^{th} harmonic by $\rho g A^n R^{3-n}$.

Case	F_1 [-]	F_2/F_1	F_3/F_1	F_4/F_1	F_5/F_1
Stansberg experiments (kA=0.28)	6.01	6.35%	2.54%	1.16%	0.25%
CFD model of Stansberg experiments (kA=0.28)	5.57	4.66%	1.71%	0.53%	0.09%

Table 3: Normalised first harmonic and ratio of higher harmonics relative to the first harmonic of the inline load on a vertical cylinder, from the Stansberg (1997) experiments and the CFD model.

Tab. 3 indicates that the agreement is excellent between Stansberg experiments and the CFD model for the first harmonic. For the higher order harmonics, the agreement is fairly good with comparable order of magnitude and trends between the different harmonics.

All the studies mentioned above deal with the total load on the cylinder. CFD allows a precise analysis of the evolution of the load with water depth as exemplified in the following section, an information difficult to obtain experimentally.

5.2. Physical analysis of the influence of the interface on two slices

Section 4.2.2 showed that the closer the slice is to the interface, the larger the bump before the wave load trough. In this section, to explain the physical origin of the hump, a study is specifically carried out on two slices: the submerged slice centred at $z = -0.225\,\mathrm{m}$ and the slice in the interface region centred at $z = -0.025\,\mathrm{m}$ (Fig. 12).

Each slice is divided into two parts to evaluate the load distribution on it: an upstream part and a downstream part as shown in Fig. 21.

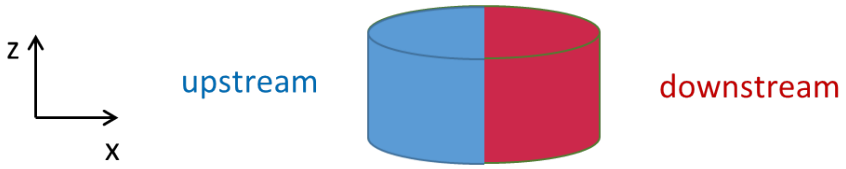

Figure 21: Slice divided into an upstream and a downstream part.

The inline force F_x along the (Ox) direction is calculated over each part, as well as the total inline force over the entire slice. In addition, the transverse force along the (Oy) direction is provided. All these forces are plotted over one wave period. During this same period, the wave run-up around the cylinder is visualised using the 0.5 iso-surface of the VOF volume fraction. For clarity, only half of the NWT is displayed, being cut at its centre by the (xOz) plane. The key moments over one period (between $0s$ and T) are described in the next two subsections.

5.2.1. Slice fully submerged in water ($z = -0.225\,\mathrm{m}$)

First, the impact of the wave run-up on the load is investigated for the submerged slice located at $z = -0.225\,\mathrm{m}$. Four key moments (t1, t2, t3 and t4) are described below and shown in Fig. 22 and Fig. 23.

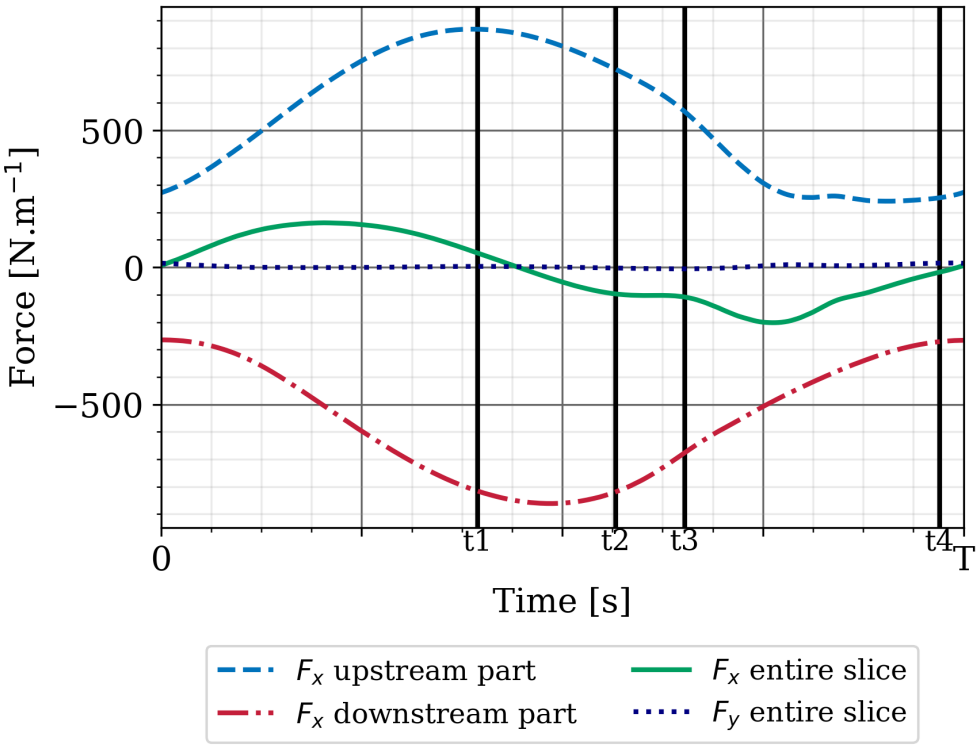

Figure 22: Wave loads on the slice centred at z=-0.225 m.

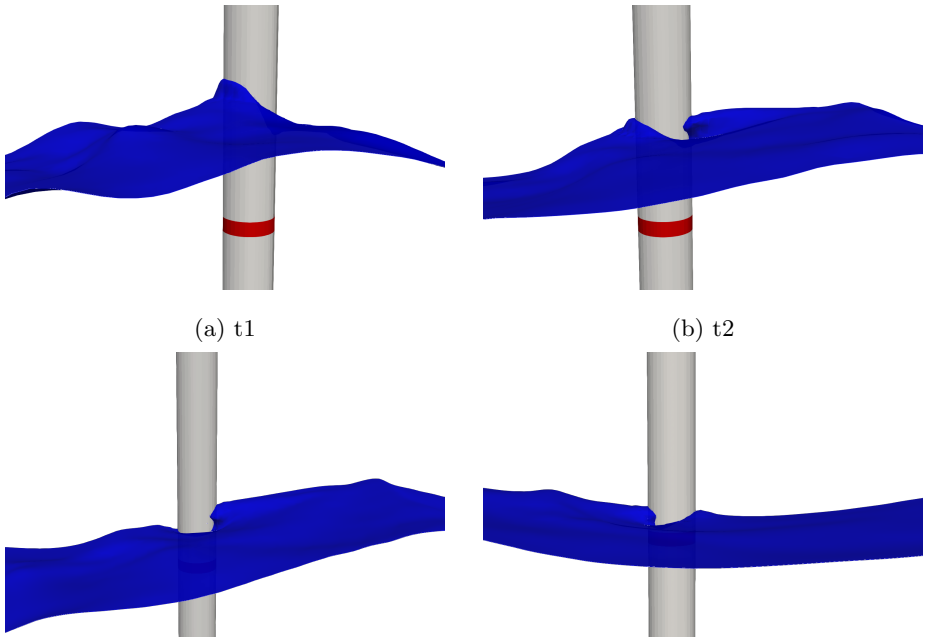

(a) t1 (b) t2

(c) t3 (d) t4

Figure 23: Visualisation of the air/water interface at four key moments for the slice located at $z = -0.225\,\mathrm{m}$. The slice over which the loads are calculated is coloured red.

- **t1**: Maximum of the inline force on the upstream part. The maximum inline load on the upstream side of the cylinder is reached exactly at the time when the run-up of the wave on the upstream part is maximum. A roll shape of the upstream wave run-up is observed. According to Paulsen et al. (2012), it is due to the stagnation pressure which accelerates a sheet of water upwards. Likewise, the maximum rise of the wave on the downstream side occurs at time (t1) just before the secondary load cycle (t2).
- **t2**: First change in the slope of the total inline force. At this point, the wave returns from downstream to upstream of the cylinder. According to Paulsen et al. (2012), this corresponds to the beginning of the secondary load cycle.
- **t3**: Second change in the slope of the total inline force. It corresponds to a change in the slope of the upstream force and to the transition from a small roll to a linear form of the wave run-up on the upstream part. From this moment on, the wave descends faster on the upstream side, which corresponds to a faster decrease of the upstream force (higher slope); this is the end of the secondary load cycle.
- **t4**: At the end of the period, the absolute value of the upstream and downstream forces are equal, giving a total force of zero on the cylinder. The free surface is almost flat and hardly disturbed by the cylinder.

From these observations, there is a clear relationship between the wave run-up and the change in slope of

the inline load signals: the wave return from the downstream to the upstream part seems to be responsible for the slope break on the total load.

In the following subsection, the physical analysis of loads on a slice located in the interface area will be carried out to check whether similar observations can be drawn.

5.2.2. Slice near the interface ($z = -0.025\,\mathrm{m}$)

Over one wave period, eight key moments are described to analyse the wave load variations on a slice near the interface region. The loads are plotted in Fig. 24 and the air/water interface is shown in Fig. 25.

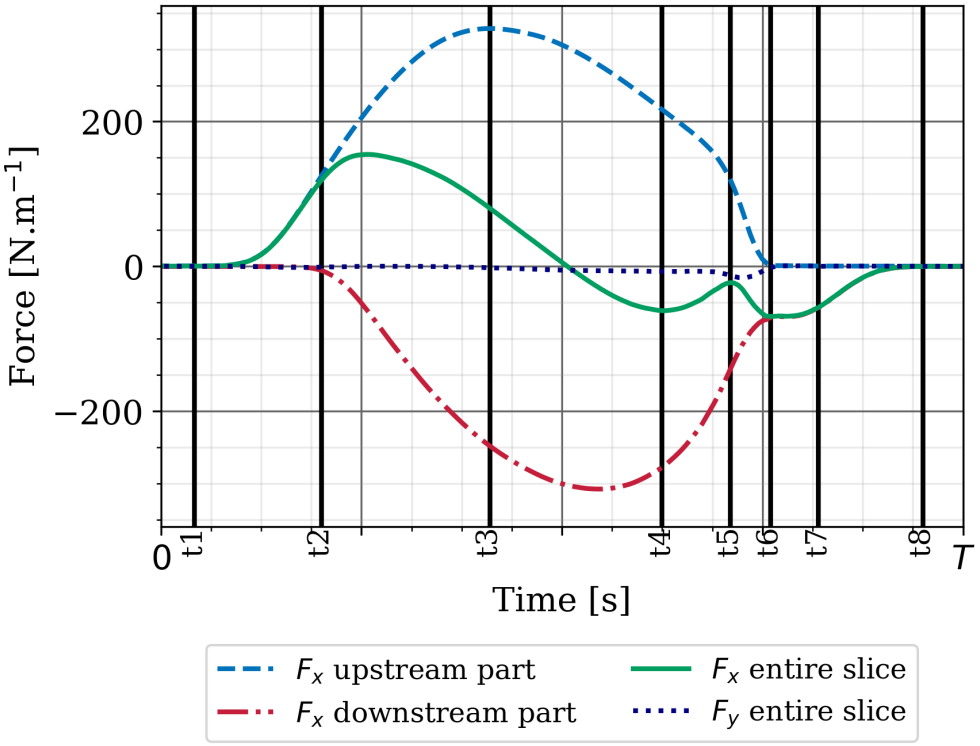

Figure 24: Wave loads on the slice centred at $z = -0.025\,\mathrm{m}$.

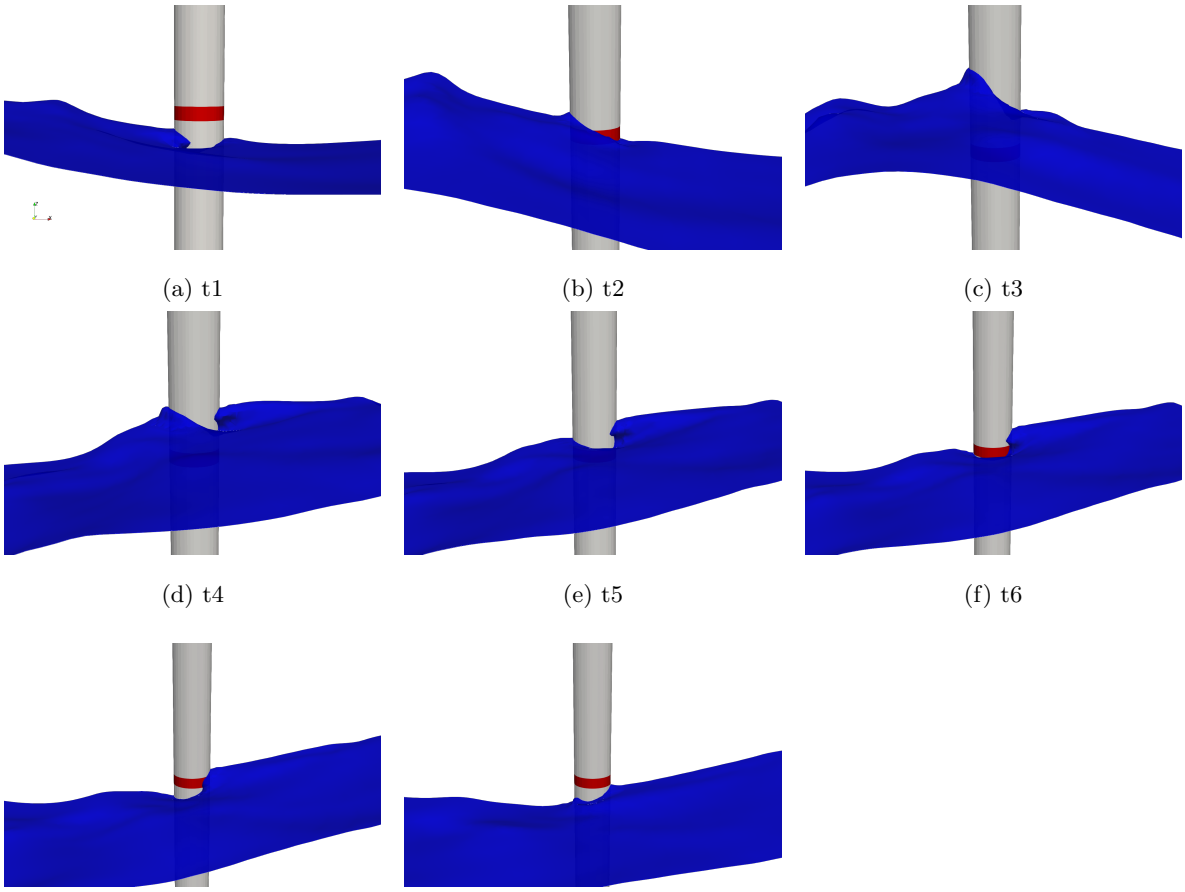

(a) t1 (b) t2 (c) t3

(d) t4 (e) t5 (f) t6

(g) t7 (h) t8

Figure 25: Visualisation of the air/water interface at height key moments for slice $z = -0.025\,\mathrm{m}$. The slice on which the loads are calculated is coloured red.

- **t1**: At the beginning of the period, all forces are zero because the slice is not yet immersed in water.
- **t2**: The wave reaches the upstream part of the cylinder, which increases the upstream inline force. The downstream inline force remains zero since the downstream part of the cylinder is still in the air.
- **t3**: Maximum upstream force. As already observed for the slice centred at $z = -0.225\,\mathrm{m}$, the wave run-up is maximal on the upstream part when the maximum inline force on the upstream part is reached. A slight change of the slope of the total force is also observed.
- **t4**: First local minimum of the total inline force. A reversal of the slope of the total inline force is observed as the wave begins to flow back from the downstream to the upstream side of the cylinder. This was also noticed for the submerged slice at t2, resulting in a change in the slope of the total inline force. This phenomenon is strongly amplified here, where the slice is closer to the interface. This is the beginning of the secondary load cycle.

- **t5**: Local maximum of the total inline force. This peak occurs simultaneously with a strong change in the slope of the upstream inline force. It corresponds to the transition between the roll and the linear shape of the wave run-up on the upstream side, as noticed for the submerged slice. In addition, a small transverse force is noticeable whereas it was negligible until now. This might be explained by the asymmetry of the flow around the cylinder when the wave recedes.
- **t6**: From t6, the upstream part is no longer immersed, the corresponding force is zero.
- **t7**: Decrease in downstream inline force. The wave descends and eventually passes under the slice, resulting in zero total force on the slice.
- **t8**: The total inline load is again zero when the slice is no longer immersed in water.

Finally, the particular variation of the wave loads (change or reversal of slope) is strongly linked to the wave run-up. The detailed temporal description allows to identify precisely the secondary load cycle, which can be explained by the backflow of the wave from the downstream part to the upstream part. This phenomenon has a greater impact on the upstream part of the cylinder than on the downstream part.

6. Conclusion

In this study, a Numerical Wave Tank using the open-source CFD tool OpenFOAM was implemented and validated in the simple case of a vertical cylinder submitted to regular waves, based on the Stansberg (1997) experiments. First, the accuracy of the CFD wave-only model was ascertained. In particular, the response of the NWT in terms of wave elevation was validated by comparison with experiments. Only negligible damping and reflection phenomena were observed along the NWT. The velocity profile along the water depth was also compared to the corresponding theoretical profile. The use of the Stokes 3^{rd} order formula coupled with an extrapolated stretching model leads to a good agreement with the velocity profile calculated by CFD, except for a slight overestimation of the velocity at the wave crest in the CFD simulations.
Then, the validity of the CFD model with the cylinder included in the NWT was assessed. Though the flow is turbulent ($Re = 10^5$), the experimentally-measured forces are correctly estimated by the NWT without a turbulence model and with a no-slip boundary condition on the cylinder.
A method, inspired by the experimental method, has been developed to derive the Morison coefficients from the CFD loads. In contrast to experiments, the variation of loads along the cylinder is taken into account by slicing the cylinder along its axis. The validity of this so-called slice methodology has been demonstrated for the simple case of a vertical cylinder piercing the free surface. This method, which gives access to local information, has made it possible to provide a detailed physical analysis of global phenomena that are already well known (appearance of non-linearity in the total forces explained by local phenomena near the interface). In the case studied, the inertia term of Morison's formula is strongly predominant and the drag term is negligible, which makes the determination of the latter rather unreliable. The coefficient of inertia varies

slightly along the submerged part of the cylinder ($C_M = 2.00 \pm 0.22$). The total load, obtained by applying Morison formula for each slice with $C_M = 2.00$ (and $C_D = 0.33$), is in good agreement with the experimental and numerical loads. Only the non-linear behaviour before the minimum of the load signal, caused by the interaction with the air/water interface, is not correctly captured by the forces calculated from the Morison formula. Indeed, the forces are strongly affected in the air/water interfacial zone, where Morison's approach is no longer valid. However, the influence of the interface remains negligible on the total load.
The non-linearity effect induced by the interface, also called secondary load cycle, has been thoroughly detailed. The slice methodology allows access to the local loads and the CFD simulation provides access to the flow structure, which helps to correlate the local phenomenon with the non-linear behaviour. In particular, a backflow of the wave from the downstream to the upstream part of the cylinder has been demonstrated, and is responsible for the non-linear shape of the total wave load.

Finally, the objective of this study was to apply the slice methodology to a simple case for which the results are known, in order to verify that the results of the method are consistent. This first step was necessary because the methodology to be implemented is complex and the sources of uncertainties or errors are numerous: implementation of the CFD simulation (two-phase flow, wave generation and propagation, interaction of the flow with a fixed structure), implementation of the post-processing in order to obtain the Morison coefficients taking into account the spatial variations. In the future, this methodology will be extended to a very complex floater composed of multiple inclined, submerged or surface piercing cylinders. The effect of the interactions between the cylinders, their inclination and their proximity to the free surface will be studied on the basis of the methodology developed in this article.

References

Afshar, M.A., 2010. Numerical wave generation in openfoam® .

Benitz, M., 2016. Simulating the hydrodynamics of offshore floating wind turbine platforms in a finite volume framework .

Benitz, M.A., Schmidt, D.P., Lackner, M.A., Stewart, G.M., Jonkman, J., Robertson, A., 2015. Validation of hydrodynamic load models using cfd for the oc4-deepcwind semisubmersible, in: International Conference on Offshore Mechanics and Arctic Engineering, American Society of Mechanical Engineers. p. V009T09A037.

Boccotti, P., 2014. Wave mechanics and wave loads on marine structures. Butterworth-Heinemann.

Borràs Nadal, A., Bozonnet, P., 2020. Surge decay cfd simulations of a tension leg platform floating wind turbine doi:10.13140/RG.2.2.14518.24641.

Bozonnet, P., Emery, A., et al., 2015. Cfd simulations for the design of offshore floating wind platforms encompassing heave plates, in: The Twenty-fifth International Ocean and Polar Engineering Conference, International Society of Offshore and Polar Engineers.

Bruinsma, N., 2016. Validation and application of a fully nonlinear numerical wave tank .

Burmester, S., Gueydon, S., Vaz, G., el Moctar, B., 2017. Surge decay simulations of a semi-submersible floating offshore wind turbine, in: Proceedings of the 20th numerical towing tank symposium, pp. 2–3.

Chakrabarti, S., 1979. Wave forces on vertical array of tubes, in: Proc. Civil Eng. Ocean, pp. 241–259.

Chakrabarti, S., 2005. Handbook of Offshore Engineering (2-volume set). Elsevier.

Chaplin, J., Rainey, R., Yemm, R., 1997. Ringing of a vertical cylinder in waves. Journal of Fluid Mechanics 350, 119–147.

Chaplin, J., Subbiah, K., 1997. Large scale horizontal cylinder forces in waves and currents. Applied Ocean Research 19, 211–223. doi:10.1016/s0141-1187(97)00021-7.

Chen, L., Stagonas, D., Santo, H., Buldakov, E., Simons, R., Taylor, P., Zang, J., 2019. Numerical modelling of interactions of waves and sheared currents with a surface piercing vertical cylinder. Coastal Engineering 145, 65–83. doi:10.1016/j.coastaleng.2019.01.001.

Clément, C., Bozonnet, P., Vinay, G., Nadal, A.B., Pagnier, P., Réveillon, J., 2020. Numerical wave tank including a fixed vertical cylinder subjected to waves, towards the investigation of floating offshore wind turbine hydrodynamics, in: Volume 6A: Ocean Engineering, American Society of Mechanical Engineers. doi:10.1115/omae2020-18797.

Faltinsen, O.M., Newman, J.N., Vinje, T., 1995. Nonlinear wave loads on a slender vertical cylinder. Journal of Fluid Mechanics 289, 179–198. doi:10.1017/s0022112095001297.

Ferrant, P., 1998. Fully nonlinear interactions of long-crested wave packets with a three dimensional body, in: Proc. 22nd ONR Symposium on Naval Hydrodynamics, pp. 403–415.

Greenshields, C.J., 2020. Openfoam user guide. OpenFOAM Foundation Ltd, version 3, e2888.

Grue, J., 2002. On four highly nonlinear phenomena in wave theory and marine hydrodynamics. Applied ocean research 24, 261–274.

GWEC, 2021. Global wind report 2021. Global Wind Energy Council .

Higuera, P., Losada, I.J., Lara, J.L., 2015. Three-dimensional numerical wave generation with moving boundaries. Coastal Engineering 101, 35–47. doi:10.1016/j.coastaleng.2015.04.003.

Huseby, M., Grue, J., 2000. An experimental investigation of higher-harmonic wave forces on a vertical cylinder. Journal of fluid Mechanics 414, 75–103.

Jacobsen, N., 2017. waves2foam manual. Deltares, The Netherlands .

Keulegan, G.H., Carpenter, L.H., et al., 1958. Forces on cylinders and plates in an oscillating fluid. Journal of research of the National Bureau of Standards 60, 423–440.

Kristiansen, D., Faltinsen, O., 2008. A study of wave loads on fixed horizontal cylinders in the free surface, in: Proceedings of the 8th International Conference on Hydrodynamics, pp. 1–9.

Larsen, B.E., Fuhrman, D.R., 2018. On the over-production of turbulence beneath surface waves in reynolds-averaged navier–stokes models. Journal of Fluid Mechanics 853, 419–460. doi:10.1017/jfm.2018.577.

Larsen, B.E., Fuhrman, D.R., Roenby, J., 2019. Performance of interFoam on the simulation of progressive waves. Coastal Engineering Journal 61, 380–400. doi:10.1080/21664250.2019.1609713.

Malenica, S., Molin, B., 1995. Third-harmonic wave diffraction by a vertical cylinder. Journal of Fluid Mechanics 302, 203–229. doi:10.1017/s0022112095004071.

Massie, W., Journée, J., 2001. Offshore hydromechanics. Delft University of Technology: Delft, The Netherlands .

Méhauté, B.L., 1976. Similitude in coastal engineering. Journal of the waterways, harbors and coastal engineering division 102, 317–335.

Miquel, A., Kamath, A., Chella, M.A., Archetti, R., Bihs, H., 2018. Analysis of different methods for wave generation and absorption in a CFD-based numerical wave tank. Journal of Marine Science and Engineering 6, 73. doi:10.3390/jmse6020073.

Morison, J., Johnson, J., Schaaf, S., et al., 1950. The force exerted by surface waves on piles. Journal of Petroleum Technology 2, 149–154.

Pan, J., Ishihara, T., 2019. Numerical prediction of hydrodynamic coefficients for a semi-sub platform by using large eddy simulation with volume of fluid method and richardson extrapolation. Journal of Physics: Conference Series 1356, 012034. doi:10.1088/1742-6596/1356/1/012034.

Paterson, E., 2008. Multiphase and free surface flow simulations, in: Third OpenFOAM workshop, Politecnico di Milano, Milan, Italy.

Paulsen, B., Bredmose, H., Bingham, H., 2012. Accurate computation of wave loads on a bottom fixed circular cylinder .

Paulsen, B.T., 2013. Efficient computations of wave loads on offshore structures. Ph.D. thesis. Technical University of Denmark.

Paulsen, B.T., Bredmose, H., Bingham, H.B., 2014. An efficient domain decomposition strategy for wave loads on surface piercing circular cylinders. Coastal Engineering 86, 57–76. doi:10.1016/j.coastaleng.2014.01.006.

Rainey, R., 2007. Weak or strong nonlinearity: the vital issue. Journal of Engineering Mathematics 58, 229–249.

Rivera-Arreba, I., Bruinsma, N., Bachynski, E.E., Viré, A., Paulsen, B.T., Jacobsen, N.G., 2019. Modeling of a semisubmersible floating wind platform in severe waves, in: International Conference on Offshore Mechanics and Arctic Engineering, American Society of Mechanical Engineers. p. V009T13A002.

Robertson, A., Wendt, F., Jonkman, J., Popko, W., Vorpahl, F., Stansberg, C.T., Bachynski-Polić, E., Bayati, I., Beyer, F., Vaal, J., Harries, R., Yamaguchi, A., Shin, H., Kim, B., Zee, T., Bozonnet, P., Aguilo, B., Bergua, R., Qvist, J., Bouy, L., 2015. OC5 project phase I: Validation of hydrodynamic loading on a fixed cylinder.

Sarlak, H., Pegalajar-Jurado, A., Bredmose, H., 2018. Cfd simulations of a newly developed floating offshore wind turbine platform using openfoam.

Sarmiento, J., Guanche, R., 2018. Introduction to offshore wind fixed stuctures. Environmental Hydraulics Institude Universidad de Cantabria.

Sarpkaya, T., 1977. In-line and transverse forces on cylinders in oscillatory flow at high reynolds numbers. Journal of ship Research 21, 200–216.

Stansberg, C., 1997. Comparing ringing loads from experiments with cylinders of different diameters—an empirical study, in: BOSS ‘97 Conference.

Sumer, B.M., et al., 2006. Hydrodynamics around cylindrical strucures. volume 26. World scientific.

Tao, L., Cai, S., 2004. Heave motion suppression of a spar with a heave plate. Ocean Engineering 31, 669–692. doi:10.1016/j.oceaneng.2003.05.005.

Tao, L., Lim, K.Y., Thiagarajan, K., 2004. Heave response of classic spar with variable geometry. Journal of Offshore Mechanics and Arctic Engineering 126, 90–95. doi:10.1115/1.1643085.

Tao, L., Molin, B., Scolan, Y.M., Thiagarajan, K., 2007. Spacing effects on hydrodynamics of heave plates on offshore structures. Journal of Fluids and Structures 23, 1119–1136. doi:10.1016/j.jfluidstructs.2007.03.004.

Tran, T.T., Kim, D.H., 2015. The coupled dynamic response computation for a semi-submersible platform of floating offshore wind turbine. Journal of wind engineering and industrial aerodynamics 147, 104–119.

Veritas, D.N., 2010. Dnv-rp-c205 environmental conditions and environmental loads. Det Norske Veritas: Oslo, Norway .

Wang, L., Robertson, A., Jonkman, J., Yu, Y.H., et al., 2020a. Uncertainty assessment of cfd investigation of the nonlinear difference-frequency wave loads on a semisubmersible fowt platform. Sustainability 13, 1–1.

Wang, Y., Chen, H.C., Vaz, G., Burmester, S., et al., 2020b. Cfd simulation of semi-submersible floating offshore wind turbine under regular waves, in: The 30th International Ocean and Polar Engineering Conference, International Society of Offshore and Polar Engineers.

Weller, H.G., 2008. A new approach to vof-based interface capturing methods for incompressible and compressible flow. OpenCFD Ltd., Report TR/HGW 4.

Wheeler, J., et al., 1970. Method for calculating forces produced by irregular waves. Journal of petroleum technology 22, 359–367.

Windt, C., Davidson, J., Schmitt, P., Ringwood, J., 2019. On the assessment of numerical wave makers in CFD simulations. Journal of Marine Science and Engineering 7, 47. doi:10.3390/jmse7020047.

Wolfram, J., Naghipour, M., 1999. On the estimation of morison force coefficients and their predictive accuracy for very rough circular cylinders. Applied Ocean Research 21, 311–328. doi:10.1016/s0141-1187(99)00018-8.

Yan, M., Ma, X., Bai, W., Lin, Z., Li, Y., 2020. Numerical simulation of wave interaction with payloads of different postures using OpenFOAM. Journal of Marine Science and Engineering 8, 433. doi:10.3390/jmse8060433.

Zhang, S., Ishihara, T., 2018. Numerical study of hydrodynamic coefficients of multiple heave plates by large eddy simulations with volume of fluid method. Ocean Engineering 163, 583–598. doi:10.1016/j.oceaneng.2018.03.060.